Shape-Based Methods for Motor Function Analysis

Shashwat Kumar

A Dissertation submitted to the Graduate Faculty
of the University of Virginia in Candidacy for the Degree of
Doctor of Philosophy

Department of Systems Engineering

University of Virginia
August 2024

Approved July 2024 by the Graduate Supervisory Committee:

Laura Barnes, Advisor
Afsaneh Doryab
Seokhyun Chung
Nikolaos Sidiropoulos
Anuj Srivastava

Shape-Based Methods for Motor Function Analysis

Shashwat Kumar

(ABSTRACT)

Problems in biomechanics often involve nuisance variables such as varying motion speeds, orientations, and individual differences in limb sizes. In order to effectively learn from smaller, noisy datasets, these factors must be quotiented out. This dissertation introduces new tools from statistical shape analysis to address such issues. In the first study, motion trajectories in children with Duchenne Muscular Dystrophy (DMD) and Spinal Muscular Atrophy (SMA) are temporally aligned using the square root of their derivative (SRVF) and analyzed with Functional Principal omponent analysis (FPCA). The results reveals key variations in curl speed and asymmetry, with SMA patients showing greater activation of the asymmetry pattern. In the second study, Kinematic and EMG data in stroke patients are analyzed using the Transported SRVF framework in Kendall shape space, improving registration and classification of hemiplegic gaits. This approach identifies mean temporal shapes and modes of variation, enhancing the understanding of gait abnormalities and potentially informing better clinical assessments. These methods improve motion analysis in children with neuromuscular disorders and stroke patients, and holds promise for developing objective motor function assessments in clinical and remote settings.

Acknowledgments

I would like to acknowledge my parents Varun Kishore Thakur and Kanchan Thakur for giving me the freedom to pursue my intellectual curiosities, my sister Amrita for showing me what grace under adversity looks like. I had not initially planned a career in academia and had a rather unusual path to it, but having been in the company of some excellent researchers (and equally amazing friends) made me change my mind: Dr. Vishaka Datta, Dr. Pawan Nandakishore, Dr. Akshit Goyal and Dr. Amit Vutha. My close friends Sowrabh and Subhash who have continued to inspire me, my girlfriend Mansi who has been my pillar of support in these times. At UVA, i have been fortunate to have amazing friends with whom I have had some most fruitful discussions: Dr. Debajyoti Datta, Dr. Arash Tavakoli, Elena Martynova, Dr. Robert Gutierrez, my labmate Arafat Rahman who has been an amazing collaborator. Finally, I would like to thank my advisor Dr. Laura Barnes for giving me this great opportunity, Dr. Tom Fletcher for teaching an amazing course on a topic as abstract as differential geometry, Dr. Nikolaos Sidiropoulos for teaching me rigor through his course, Dr. Steven Boker for showing me how to be a good human being alongside being a good scientist. Finally, I am especially indebted to Dr. Pierre-Antoine Absil and Dr. Anuj Srivastava for their mentorship in my academic journey.

Contents

List of Figures **vii**

List of Tables **xi**

1 Introduction **1**

1.1 Organization 3

2 Riemannian Geometry Tools **4**

2.0.1 SRVF: Invariance to reparameterizations of time 7

2.0.2 Kendall Shape Space TSRVF: Invariance to translation, rotation, scaling and reparameterizations of time 8

2.0.3 Kendall TSRVF invariances 10

3 An Interpretable Shape Based Index For Pediatric Motor Function **12**

3.1 Introduction 12

3.2 Method 15

3.2.1 Experimental Protocol 15

3.2.2 Curve Registration and Shape PCA 16

3.2.3 Statistical Analyses 19

3.3 Results 20

3.3.1 Overview of the Approach 20

3.3.2 Insights from Curve Registration 21
3.3.3 Discovering Modes of Variation in Trajectories 22
3.3.4 Analyzing Cohort Differences 24
3.3.5 Insights from Cross Correlation 25
3.3.6 Combining Modes of Variation 27
3.3.7 Comparison with other Decomposition Techniques 28
3.3.8 Mixed-Effects Regression 29
3.4 Discussion and Future Work 30

4 Jointly Analyzing Emg and Motion Shapes for Understanding Motor Function Rehabilitation in Stroke 33

4.1 Introduction 33
4.2 Related Work 35
4.3 Methodology 35
4.3.1 Kendall Shape Space based transported srvf formulation 35
4.4 Results 40
4.5 Discussion 48

5 Conclusions 50

Bibliography 53

List of Figures

2.1 a) Simple example of a quotient space. a) Construction of circle by ”gluing” together end points of a line. b) Construction of a torus by defining edges to be equivalent. 5

2.2 All these 3 skeletons form the same shape in kendall shape space 9

3.1 Overview of the study and the proposed shape analysis pipeline. Wearable sensors capture physiological signals from participants performing activities of daily living. This data is combined with shape analysis and external assessments to develop a canonical index of motor function. 14

3.2 Results on performing curve registration and Fréchet mean calculation with temporal matching. (a) Signals with only amplitude variability, (b) Warping functions, (c) Signals with amplitude and phase variability, (d) Signals after registration, (e) Reconstructed warping functions, (f) Euclidean and Shape mean. Note how the shape mean (blue) captures the symmetric shape better than the euclidean mean (red). 14

3.3 (a-d) Results on peforming phase amplitude separation on healthy and (e-h) DMD/SMA cohorts. 15

3.4 A simulated illustration of alignment of arm curls. (a) An example of arm curl. (b) Temporal rate or warping function of this arm curl. (c) An example of misaligned arm curls. (d) Functions after alignment. 19

3.5 (a-c) Vertical modes of variation obtained from Shape PCA on the curl data. (a) The first mode represents scaling, (b) the second asymmetry in motion while (c) the last represents noise. (d-f) Modes of variation obtained from knocking data. (d) The first mode represents scaling. (e) The second mode represents asymmetry in motion while (f) the last represents sensor noise. . . 23

3.6 Interpretation of Vertical Principal Component 2 of arm curl (VPC2 Curl) in videos of 2 participants. The participants do the downward motion of the arm curl faster than the upward motion, possibly because of some sort of compensation. 23

3.7 Boxplots of some demographic variables along with important clinical measures and feature dimensions. (a) Age, (b) Brooke score, (c) Average Echogenicity (Avg_Echo (gsv)), (d) Normalized Elbow Torque (NET (Nm/cm)), (e) VPC1 Curl (Speed), (f) VPC2 Curl (Asymmetry), (g) VPC1 Knock (Speed), and (h) VPC2 Knock (Asymmetry). 25

3.8 Pearson Cross Correlation of different VPC modes with clinical measures for DMD (N=15), SMA (N=7), and Healthy (N=9). (a) Cross correlations for VPC1 Curl (Speed), and (b) VPC1 Knock (Speed). 26

3.9 Distribution of three different principal PLS correlations (first column) and components. For first principal component, our motor function index has median correlation of $r = 0.77$ (95% CI [0.34, 0.94]) with dimensions of muscle fat infiltration (Avg_Echo), Brooke score, and Age related degenerative changes. Speed of curl (VPC1 Curl) and knock (VPC1 Knock) have tighter spread in distribution than the asymmetry features (VPC2 Curl and VPC2 Knock). 27

3.10 Comparison of different decomposition methods, (a-c) Shape PCA with alignment leads to much more interpretable modes of variation than (d-f) NMF, and (g-i) Functional PCA without alignment because of the phase variability. 28

4.1 a) Action of nuisance groups (rotation/translation/scaling/reparameterizations) obfuscates the latent periodic structure in the data and makes it challenging to perform simple tasks like computing means. b) Registering raw data with our method allows us to see this structure as well as analyze both kinematic and muscle activity shapes. 36

4.2 Example of kinematic registration. 36

4.3 Example of tsrvf construction and trajectory interpolation on a Sphere Manifold. 36

4.4 Comparison of registration with [41]. 37

4.5 Pairwise distances, block structure in healthy possibly because easier to register healthy to another healthy. Middle is registration from [41]. 37

4.6 14, 10, 36 are stroke patients close to healthy, 42, 34, 2 are stroke patients far from healthy. 37

4.7 Mean calculation from registered curves. Stroke mean shown in red while healthy shown in blue. Hemiplegic show dragging. 37

4.8 Pca modes 1 (short stride + stiffer limbs + head position up or down),7 (left arm variability), 9 (elbow variation), 14 (Right Shoulder variation). 7, 9 and 14 seem to capture differences between stroke left and right 38

4.9 Boxplots showing separation between healthy and stroke via pcs 38

4.10 Correlation of demographic with pcs 38

4.11 EMG Registration 46

4.12 First EMG Eigenfunction 47

4.13 Median F1 score and ROC AUC vs rank for classification performed on principal components achieved from registered and unregistered trajectories. Registration seems to reduce required rank for higher classification accuracy. . . 47

List of Tables

3.1 Demographics of Participants 16

3.2 Description of clinical measures against which we correlate our wearable features 19

3.3 Performance comparison for different algorithms reported in terms of bootstraped canonical correlation of each component 29

3.4 Mixed Linear Model Regression: VPC1 Curl ∼ Age * Cohort 30

3.5 Mixed Linear Model Regression: VPC2 Curl ∼ Age * Cohort 30

4.1 Performance comparison for different algorithms based on k-nearest neighbors in order to understand effect of distances on classification performance. . . . 47

4.2 Performance comparison for different algorithms with and without alignment. 47

Chapter 1

Introduction

Problems in biomechanics often involve confounders. In order to efficiently learn from smaller noisy dataset, it's important to quotient out or remove the effect of these confounders. As an example, consider a problem involving building a wearable technology to assess motor function in children with Duchenne Muscular Dystrophy (DMD) and Spinal Muscular Atrophy (SMA). As anyone who has done data collection in a pediatric setting will testify, it's difficult to get children to perform motion at a slow controlled speed, as possible with an older population. Children are often nervous or unable to follow precise instructions. Furthermore, because of the rare nature of the diseases, it's extremely difficult to collect data and it's essential to build models with parameterized invariances as opposed to building models which can learn invariances by seeing a lot of training examples (eg. a neural network learning rotational invariance by having filters at different orientations).

The problem exacerbates when working with naturalistic data. Consider another application of building a system to identify differences in hemiplegic vs normal gait. In order to understand a patient's progress post rehabilitation in stroke, it's important to focus on both motion (kinematic) and electrical activity of muscles (emg), both form and function. Joint analysis of both modalities can reveal abnormal muscle activity patterns or movement patterns like spastic gait, which are hard to obtain from a single modality. Some recent studies have started collecting gait data by allowing the participants to walk at their own natural speed, to not bias their motion ([1]). Here, similar to the previous case, there is phase variability, since different patients have different preferred motion speeds. Furthermore, there is variability in joint sizes of participants because of height differences and distance from camera (scale). Even if participants perform the same motion shape, participants who are starting off at different positions (translation) and orientation (rotations) are going to have different sensor trajectory representations. As a consequence, distances and thus machine learning systems can be sensitive to these nuisance variables.

In this disseration, we use tools from statistical shape analysis to model such problems in quotient spaces modulo a certain group. In the first problem, we model the problem with the square root of it's derivative modulo the group of reparameterizations of time. By temporally aligning arm curl trajectories, we utilize functional principal component analysis (FPCA) to identify two dominant variations: curl speed and asymmetry due to difficulty with the upward motion against gravity. Similar variations are observed in knocking motions. Both DMD and SMA patients exhibit high functional variability, with higher-functioning individuals comparable to healthy controls. Notably, patients with SMA showed significantly greater activation of the curl asymmetry pattern ($p < 0.01$). We further combined projections of these variations with Canonical Correlation Analysis (CCA) to discover a covariation mode with a canonical correlation of $r = 0.65$ with muscle fat infiltration, Brooke's score (a motor function score), and age-related degenerative changes. This CCA-derived mode is proposed as a novel motor function index. In the second work, we embed biomechanical trajectories from healthy and stroke patients in kendall shape space, which quotients out translation, rotation, scaling as well as reparameterizations of time. Registration is performed in kendall shape space which outperforms previous stroke registration methods (eg. based on OPA). This allows us to extract a mean temporal shape for each cohort, as well as identify modes of variation. A joint model is built on top of these modes of variation obtained from kinematic and emg to obtain an F1 score of 0.92.

The novel contributions of this dissertation are the following:

1. A shape based functional index for objective assessment of motor function in patients

with Duchenne Muscular Dystrophy and Spinal Muscular Atrophy.

2. A method for registration and joint shape analysis of kinematic and emg in order to identify differences and idiosyncracies in healthy and hemiplegic gaits.

1.1 Organization

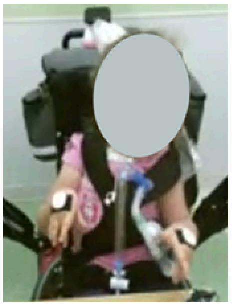

Problem: Studying motor function in children with Duchenne and SMA

Data: Angular velocity from IMU Gyroscope Sensor

Nuisance Group: Time Reparameterizations

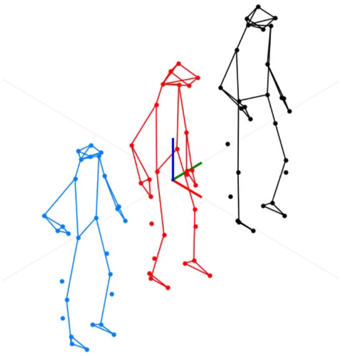

Problem: Build a system to identify differences in hemiplegic and normal gait.

Data: Kinematic data from Vicon and Emg data

Nuisance Group: Time Reparameterizations x Translation x Rotation x Scaling

Chapter 2

Riemannian Geometry Tools

Equivalence Relation

An **equivalence relation** on a set X is a binary relation, which implies

$$\forall a, b, c \in X \quad \begin{cases} a \sim a \text{ (Reflexive)} \\ a \sim b \iff b \sim a \text{ (Symmetric)} \\ (a \sim b \text{ and } b \sim c) \implies a \sim c \text{ (Transitive)} \end{cases} \tag{2.1}$$

The equivalence class of a under $\sim$ is defined as

$$[a] := \{x \in X \mid x \sim a\}$$

As an example, on the set $X = \{a, b, c\}$, the relation $R = \{(a, a), (b, b), (c, c), (b, c), (c, b)\}$ is an equivalence relation. The following sets are equivalence classes of this relation:

$$[a] = \{a\},$$

$$[b] = [c] = \{b, c\}.$$

The set of all equivalence classes for R is $\{\{a\}, \{b, c\}\}$. This set is a partition of the set X with respect to R and is also called a quotient set.

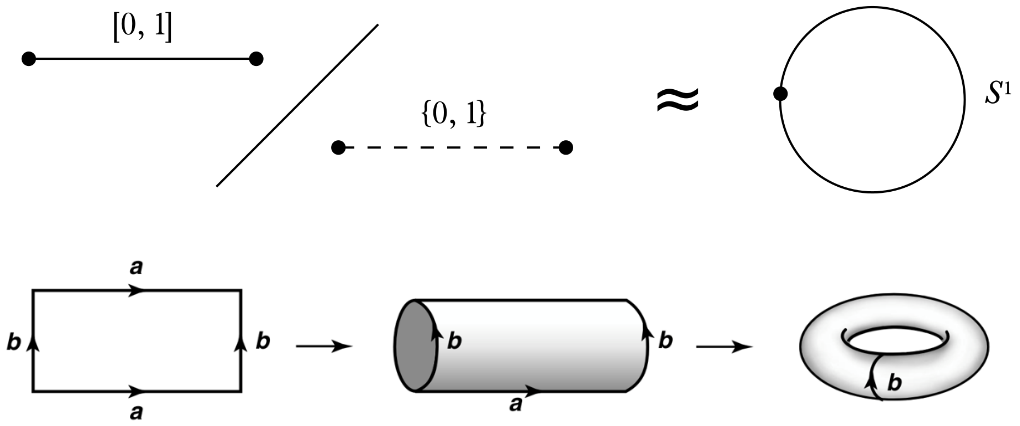

Figure 2.1: a) Simple example of a quotient space. a) Construction of circle by ”gluing” together end points of a line. b) Construction of a torus by defining edges to be equivalent.

Riemannian Metric

A **Riemannian metric** on a manifold M is a function g that assigns to each point $p \in M$ an inner product g_p on the tangent space T_pM. This inner product varies smoothly from point to point. The metric g allows us to define important geometric concepts such as:

- **Length of a curve**: The length of a curve $\gamma : [a, b] \to M$ is given by

$$L(\gamma) = \int_a^b \sqrt{g_{\gamma(t)}(\dot{\gamma}(t), \dot{\gamma}(t))}\, dt.$$

Isometry

An **isometry** between two Riemannian manifolds (M, g) and (N, h) is a diffeomorphism $\phi : M \to N$ such that ϕ preserves the metric,

$$g_p(u, u) = h_{\phi(p)}(d\phi(u), d\phi(v))$$

for all tangent vectors $u, v \in T_pM$. Isometries preserve geometric properties such as distances and angles.

As an example:

Action of Translations on R^2

$$\begin{aligned} M = R^2, N = R^2, g(u,v) = u^T v \\ \phi(p) = c + p, c \epsilon R^2 \text{ (Translation Group)} \\ d\phi = I, d\phi(u) = u, d\phi(v) = v \\ h = g \quad \text{results in an isometry} \end{aligned} \tag{2.2}$$

Shape distance computations

Let M be a Riemannian Manifold. Let d be a distance metric on M. Let G be a Lie Group which acts on M. We define the orbit of a point on the manifold

$$[x] := \{g.x \quad \forall g \epsilon G\} \tag{2.3}$$

If the Lie group G acts vis isometries, meaning that $d(x_1, x_2) = d(g.x_1, g.x_2) \quad \forall g \epsilon G, x_1, x_2 \epsilon M$, then,

$$d([x_1],[x_2]) = inf_{g_2 \epsilon G} d(x_1, g_2.x_2) \tag{2.4}$$

Some Shape Spaces and their invariances:

2.0.1 SRVF: Invariance to reparameterizations of time

Let $\beta : [0, T] \rightarrow \mathbb{R}^{\mathbb{D}}$ be an absolutely continuous function. The srvf ([2]) of the function is defined as:

$$q(\beta(t)) = \frac{\dot{\beta}(t)}{\sqrt{\|\dot{\beta}(t)\|}} \tag{2.5}$$

The space of all such q is $L^2([0,1], \mathbb{R}^D)$.

Given two functions u, v and their srvfs $q(u)$ and $q(v)$, their dot product is given by:

$$\langle q(u), q(v) \rangle = \int_0^T \frac{\dot{u}(t)}{\sqrt{\|\dot{u}(t)\|}} \frac{\dot{v}(t)}{\sqrt{\|\dot{v}(t)\|}} dt \tag{2.6}$$

$$q(u(\gamma(t))) = \frac{\dot{u}(\gamma(t))\dot{\gamma}(t)}{\sqrt{\|\dot{u}(\gamma(t))\dot{\gamma}(t)\|}} = \frac{\dot{u}(\gamma(t))\dot{\gamma}(t)}{\sqrt{\|\dot{u}(\gamma(t))\|}\sqrt{\|\dot{\gamma}(t)\|}} = q(u(\gamma(t)))\sqrt{\dot{\gamma}(t)} \tag{2.7}$$

If we reparameterize time with a function $\gamma(t)$, the action on this dot product is given by

$$\begin{aligned} \langle q(u \circ \gamma), q(v \circ \gamma) \rangle = \int_0^T q(u(\gamma(t)))\sqrt{\dot{\gamma}(t)} q(v(\gamma(t)))\sqrt{\dot{\gamma}(t)} dt &= \int_0^T q(u(\gamma(t)))q(v(\gamma(t)))\dot{\gamma}(t) dt \\ &= \int_0^T q(u(s))q(v(s)) ds = \langle q(u), q(v) \rangle \\ &\text{Where } s = \gamma(t) \end{aligned} \tag{2.8}$$

Thus angles and distances between two srvfs are invariant to action of reparameterizations of time. This makes it theoretically appealing in our first work where we need to calculate distances between trajectories performed by children which are less sensitive to the rate with which they perform the motion.

2.0.2 Kendall Shape Space TSRVF: Invariance to translation, rotation, scaling and reparameterizations of time

One well-known shape space is the **Kendall shape space**, which is used in statistical shape analysis. It represents the set of all possible shapes of a given configuration of points modulo translations, rotations, and scalings. The Kendall shape space is a quotient space obtained by factoring out these transformations, and it has a rich geometric structure that allows for the study of shape variability and comparison.

We consider the space of $m \times k$ real matrices representing our k landmarks.

$$X \epsilon \mathbb{R}^{m \times k} \tag{2.9}$$

These matrices are acted upon by the group of translations, scaling and rotations. In order to compute shape distance between skeletons, we need to remove the action of these groups.

We mean center these matrices to remove translation as a degree of freedom. This yields a new vector space where translation has been quotiented out.

$$V_m^k = \{X \epsilon \mathbb{R}^{m \times k} : \sum_{i=1}^{k} X[:, i] = 0\} \tag{2.10}$$

Scaling is quotiented out by imposing the unit frobenius norm constraint.

$$S_m^k = \{X \epsilon V_m^k : \|X\|_2 = 1\} \tag{2.11}$$

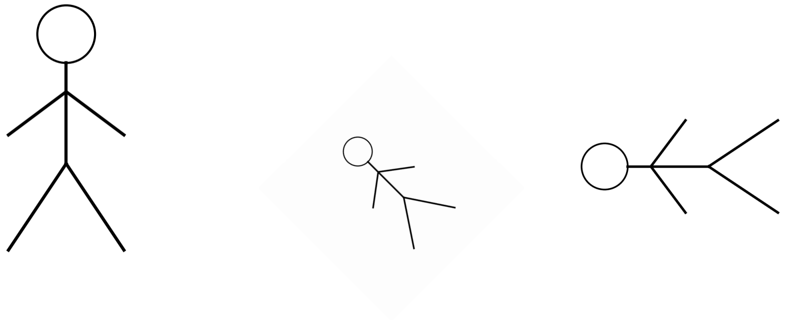

Figure 2.2: All these 3 skeletons form the same shape in kendall shape space

.

Because of the unit norm constraints, the preshape space has a spherical geometry.

This is easy to see with certain examples:

S_1^2: Consider two landmarks 1-dimensional landmarks x_1 and x_2. This is subject to the constraints $x_1 + x_2 = 0$. This yields V_1^2 as a 1 dimensional line embedded in the 2d plane. Intersection with $x_1^2 + x_2^2 = 1$ yields the space of landmarks as 0 dimensional sphere with radius 1 $S_1^2 = \{ \begin{bmatrix} \frac{1}{\sqrt{2}} & -\frac{1}{\sqrt{2}} \end{bmatrix}, \begin{bmatrix} \frac{-1}{\sqrt{2}} & -\frac{1}{\sqrt{2}} \end{bmatrix} \}$

S_1^3: V_1^3 is a 2 dimensional vector space. Intersection with the 2 sphere yields a 1 dimensional sphere as the solution

S_m^n: By a generalization of the previous argument ([3]), this is a m(n-1)-1 dimensional sphere.

Since translations and scalings have been quotiented out, our landmark matrices lying in S_m^k are acted upon by a group of rotations.

$$\mathcal{SO}(3) = \{R \in \mathbb{R}^{3\times 3} \mid R^T R = I, det(R) = 1\} \tag{2.12}$$

.

.

Rotations acts by isometries in preshape space

$$\begin{aligned} M = S^k_m, N = S^k_m, g(u,v) = t(u^T v) \\ \phi(p) = R.p, R\epsilon\mathcal{SO}(3)(\text{Special Orthogonal Group}) \\ d\phi(u) = R(p+u) - Rp = Ru, d\phi(v) = R(p+v) - Rp = Rv \\ \text{Set h=g} \\ h(d\phi(u), d\phi(v)) = t(d\phi(u)^T d\phi(v)) = t(u^T R^T R v) = t(u^T v) = g(u,v) \end{aligned} \tag{2.13}$$

We define an equivalence relation between two matrices $X_1, X_2 \epsilon S^k_m$ $X_1 \sim X_2$ if and only if $X_2 = RX_1$

This allows us to define the shape space as a quotient space under this equivalence relation

$$\Sigma^k_m = S^n_m / \sim \tag{2.14}$$

The topology and geometry of Σ^k_m is more involved, and thoroughly covered in [3].

For points away from singularities, the quotient map is a Riemannian Submersion. This allows us to define geodesics and the distance between two shapes $p_1, p_2 \epsilon \Sigma^n_m$ can be defined as

$$d(p_1, p_2) = inf_R d(X_1, R * X_2) \tag{2.15}$$

Where d is the geodesic distance on the sphere. Orthogonal Procrustes Analysis for alignment is used to find the solution to this problem.

2.0.3 Kendall TSRVF invariances

Given a curve lying in kendall shape space $\beta : [0, T] \to \Sigma^m_k$, the transported srvf is define as ([4])

$$q(\beta(t)) = \frac{\dot{\beta}(t)_{\beta_t \to c}}{\sqrt{\|\dot{\beta}(t)_{\beta_t \to c}\|}} \tag{2.16}$$

We now consider the action of transformations of the type

$$\hat{\beta}(t) = \alpha(t)R(t)\beta(t) + c(t) \tag{2.17}$$

.

In this case $q(\hat{\beta}(t)) = q(\beta(t))$.

This is because

1. $\beta(t)$ is invariant to group action of translations and scalings because of mean centering and normalization.
2. $\dot{\beta}(t)$ involves measuring changes in shape space Σ_k^m, where action of all fibers $R.\beta(t)$ has been collapsed to a single point. Thus $\dot{\beta}(t)$ and consequently $q(\beta(t))$ is invariant to action of R.
3. Distance between two tsrvfs is invariant to reparameterizations of time.

These three properties make tsrvf-kendall an extremely powerful representation in our second application, where skeleton sequences might have arbitrary rotations, translations, scalings and reparameterizations acting on them.

Chapter 3

An Interpretable Shape Based Index For Pediatric Motor Function

3.1 Introduction

Advanced medicines, including gene and cell therapies, are rapidly emerging as transformative treatments for rare and degenerative diseases. Duchenne Muscular Dystrophy (DMD), the most prevalent genetic cause of death in boys, and Spinal Muscular Atrophy (SMA), a leading genetic cause of infant mortality, have witnessed groundbreaking advancements with therapies such as Nusinersen and gene therapy [5, 6, 7]. Despite these strides, the landscape of drug development remains hindered by significant challenges, primarily due to the difficulty in recruiting large cohorts necessary for robust statistical analyses. This issue is further complicated by the subjective nature and imprecision of current trial outcome measures. These often rely on behavioral assessments, such as the Brooke Upper Extremity Scale, which measures arm function in patients with DMD [8], and the Children's Hospital of Philadelphia Infant Test of Neuromuscular Disorders (CHOP-Intend), which evaluates motor function in infants with SMA [9]. Both scales, along with other observational methods, are susceptible to clinical bias and may not capture subtle changes critical for evaluating treatment efficacy [10].

The emergence of wearable-based motion assessments presents a promising solution to these challenges. By embedding sensors into everyday activities, continuous, home-based monitoring becomes feasible, offering a holistic view of patient health beyond sporadic clinical visits [11, 12, 13, 14]. This approach facilitates the collection of longitudinal data with greater ease and frequency, enabling more accurate tracking of disease progression and treatment effects over time. In contrast to traditional methods that rely on intermittent clinical evaluations, wearable sensors allow for the seamless gathering of comprehensive movement data in a naturalistic setting, reducing the burden on patients and their families.

However, pediatric movement data is inherently complex, due to confounding factors such as limb length variations in growing children, variability in movement speed, and differing cognitive abilities. These issues can significantly alter movement trajectory representations, complicating the analysis and comparison of motion trajectories, especially in a young population where consistent movement speeds are difficult to achieve [15, 16]. Robust methods for temporal alignment are essential to accurately compare and analyze these trajectories and understand variables like disease progression.

Moreover, many existing classifiers in digital medicine rely on black-box features, making it challenging for clinicians to trust their outputs [17, 18, 19]. In contrast, our framework utilizes Shape-based Principal Component Analysis to simultaneously temporally align movement trajectories and quantify patient behavior in terms of interpretable shape-based phenotypes [2, 20, 21, 22]. This method identifies and correlates specific movement patterns with clinical metrics such as muscle fat infiltration and motor function scores. By providing transparent and intuitive results, our approach has the potential to provide objective feedback of treatment progress compared to existing methods.

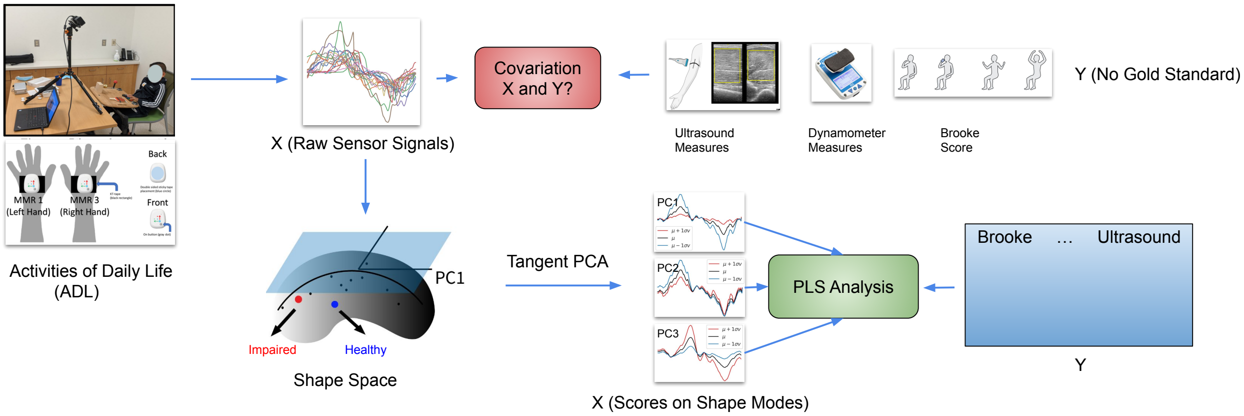

Figure 3.1: Overview of the study and the proposed shape analysis pipeline. Wearable sensors capture physiological signals from participants performing activities of daily living. This data is combined with shape analysis and external assessments to develop a canonical index of motor function.

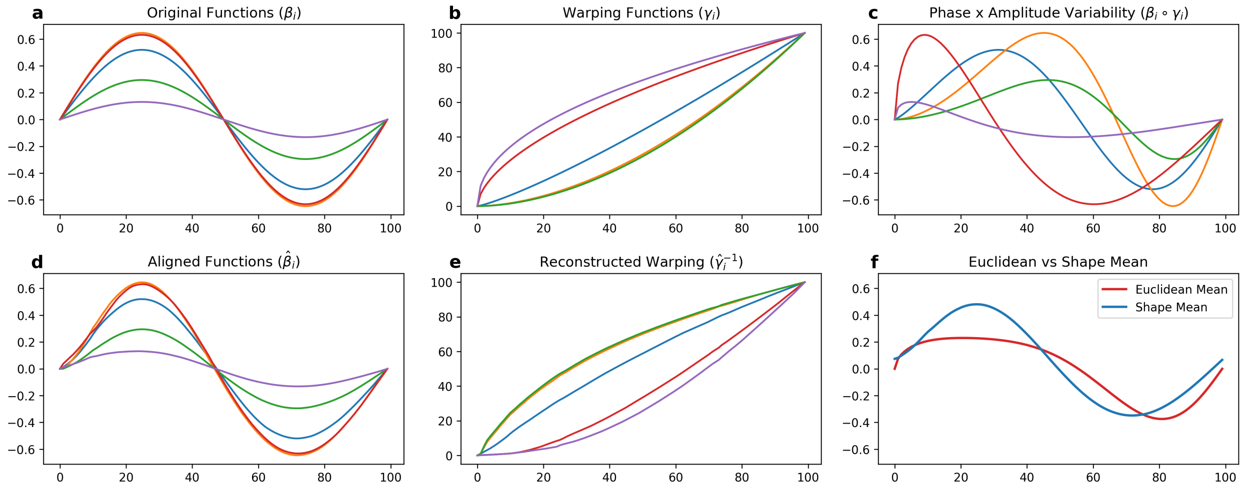

Figure 3.2: Results on performing curve registration and Fréchet mean calculation with temporal matching. (a) Signals with only amplitude variability, (b) Warping functions, (c) Signals with amplitude and phase variability, (d) Signals after registration, (e) Reconstructed warping functions, (f) Euclidean and Shape mean. Note how the shape mean (blue) captures the symmetric shape better than the euclidean mean (red).

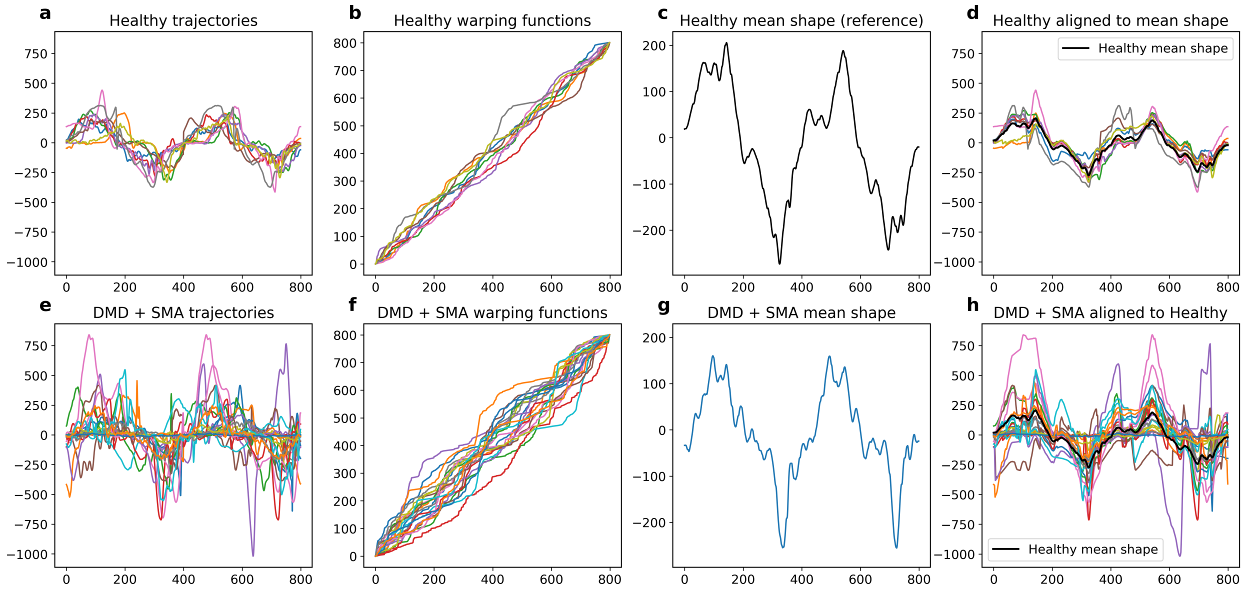

Figure 3.3: (a-d) Results on peforming phase amplitude separation on healthy and (e-h) DMD/SMA cohorts.

3.2 Method

3.2.1 Experimental Protocol

This study, approved by the University of Virginia's Institutional Review Board for Health Sciences Research (protocol #12161), recruited participants through the Pediatric Neuromuscular Clinic at the University of Virginia Children's Hospital [23]. Patients diagnosed with either SMA or DMD participated, along with age and sex-matched healthy controls (±1 year) (n = 13). All participants' demographic data are shown in Table 3.1. Participants wore MetaMotionR+ (MbientLab, San Francisco, CA, USA) sensors on both dominant and non-dominant hands, with accelerometer and gyroscope data collected at 200 Hz [24]. Activities of daily living (ADLs) including rotating door knob, raising cup, arm curl, door knocking, and moving paddle were performed by the participants. The Brooke Upper Extremity Scale was employed to provide a standardized metric for comparison across all cohorts [8]. Following data processing, a subset of participants were excluded from subsequent analysis due to sensor malfunction (n = 2), young age and refusal to cooperate (n = 2), deceased (n =

Table 3.1: Demographics of Participants

Cohort	**Number**	**Age Range**	**Mean Age**	**Sex**
Control	13	2-35	15.2	8M, 5F
SMA	9	2-19	7.4	2M, 7F
DMD	19	4-35	14.2	18M, 1F

1), participant withdrawal (n = 1), or lack of discernible motion (n = 4). This resulted in a final analysis dataset of 31 participants (DMD = 15, SMA = 7, Healthy = 9). Considering the rarity of both SMA and DMD, this sample size is considered relatively large for studies investigating these conditions.

3.2.2 Curve Registration and Shape PCA

Let $\{\beta_i : [0, T] \to \mathbb{R},\ i = 1, 2, \ldots, n\}$ be the set of curves representing motions for n subjects. In our case, it represents the gyroscope signals of y-axis. The gyroscope was selected because it measures angular velocity, which reduces the impact of significant variations in limb length. Our goal is to perform temporal alignment and phase-amplitude separation of these curves. The temporal alignment of a curve is based on a time-warping function $\gamma : [0, T] \to [0, T]$ that has the following properties. A γ is smooth, strictly increasing (i.e., its derivative is strictly positive), and is invertible with a smooth inverse. Furthermore, $\gamma(0) = 0$ and $\gamma(T) = T$. Such functions are called *positive diffeomorphisms* or *phases* and help facilitate temporal alignments. Let the set of all time-warping functions be Γ. For a curve β_i and a $\gamma \in \Gamma$, the composition $\beta_i(\gamma(t))$ or $(\beta_i \circ \gamma)(t)$ defines the time warping of β_i by γ.

We begin the alignment approach using the pairwise problem. Given two curves, β_1 and β_2, we seek a time warping function γ_2 such that the peaks and valleys in $\beta_2 \circ \gamma_2$ are optimally aligned to those of β_1. Historically, one would use the optimization $\arg\min_{\gamma \in \Gamma} \|\beta_1 - \beta_2 \circ \gamma\|$ to solve the alignment problem, where $\|f\| = \sqrt{\int_0^T f(t)^2\ dt}$ represents the classical $\mathbb{L}^2$ norm. In practice, the $\mathbb{L}^2$ of a function is approximated using a finite sum from its uniformly-sampled points, $\|f\| \approx \sqrt{(\frac{T}{J}\sum_{j=1}^{J} f(t_j)^2)}$. However, this optimization has several mathematical and computational shortcomings, and a modern approach utilizes the concept of Square-Root Velocity Functions (SRVFs). The SRVF of a curve β_i is given by $q_i(t) \doteq \text{sign}(\dot{\beta}_i(t))\sqrt{|\dot{\beta}_i(t)|}$. If we time warp a curve β_i into $\beta_i \circ \gamma$, then the SRVF of the new curve is given by $(q_i \circ \gamma)\sqrt{\dot{\gamma}}$. This sets up the so-called *elastic* approach to curve alignment. The optimal alignment of β_2 to β_1 is given by solving the optimization problem:

$$\gamma_2 = \arg\min_{\gamma \in \Gamma} \|q_1 - (q_2 \circ \gamma)\sqrt{\dot{\gamma}}\|^2 \ , \tag{3.1}$$

where q_1, q_2 are SRVFs of β_1, β_2, respectively. This optimization is solved using the efficient Dynamic Programming Algorithm (DPA) [25]. Figure 3.4 illustrates this optimization where Figure 3.4a shows an example of arm curl β_1 and Figure 3.4b shows the temporal rate or warping function γ_1 of that arm curl. Figure 3.4c shows two misaligned curves β_1, β_2, and Figure 3.4d shows the aligned curves β_1 and $\beta_2 \circ \gamma_1^{-1}$. The minimum value in Eqn. 3.1 results in distance between the shapes of β_1 and β_2:

$$d_a(\beta_1, \beta_2) = inf_{\gamma_2}\|q_1 - q_2 \circ \gamma_2\sqrt{\dot{\gamma}_2}\| \tag{3.2}$$

An important property of this distance is that it is unchanged by arbitrary time warpings of β_1 and β_2. That is,

$$d_a(\beta_1, \beta_2) = d_a(\beta_1 \circ \gamma_a, \beta_2 \circ \gamma_b), \quad \text{for any} \quad \gamma_a, \gamma_b \in \Gamma \ .$$

Therefore, it can be used to compare biomechanical signals without any influence of the rates at which the activities are performed.

This pairwise alignment can now be extended to align multiple curves and to separate their phases and amplitudes.

$$\hat{\mu}_n \doteq \arg\min_{q \in \mathbb{L}^2} \left(\sum_{i=1}^{n} \left(\min_{\gamma_i \in \Gamma} \| q - (q_i \circ \gamma_i)\sqrt{\dot{\gamma}_i} \|^2 \right) \right) . \tag{3.3}$$

This optimization is solved iteratively. Each iteration includes two steps: (1) aligning individual SRVFs q_is to the current $\hat{\mu}_n$ using Eqn. 3.1 repeatedly and (2) Updating the estimate of μ using cross-sectional average of current aligned SRVFs according to:

$$\hat{\mu}_n \mapsto \frac{1}{n} \sum_{i=1}^{n} (q_i \circ \gamma_i)\sqrt{\dot{\gamma}_i} .$$

We stop the iteration when the updates result in small changes. The FDASRSF[1] [26] provides implementations of this solution in matlab, python, and R. The outputs of this procedure are: (1) $\hat{\mu}_n$: the overall mean shape of the given curves, (2) $\{\gamma_i^*\}$: the phases that align individual curves to the mean shape, and (3) $\{\tilde{\beta}_i = \beta_i \circ \gamma_i^*\}$: the set of aligned curves or amplitudes of the original curves. In summary, each individual curve β_i is decomposed into its phase γ_i^* and amplitude $\tilde{\beta}_i$ such that $\beta_i = \tilde{\beta}_i \circ \gamma_i^*$. Figure 3.3 shows examples of this separation. In each row, the first column shows the original data (Figure 3.3a and e), the second column shows the phases $\{\gamma_i^*\}$ (Figure 3.3b and f), the third column shows the mean $\hat{\mu}_n$ (Figure 3.3c and g), and finally the last column shows the aligned amplitudes $\{\tilde{\beta}_i\}$ (Figure 3.3d and h). The aligned functions $\{\tilde{\beta}_i\}$ represent the shapes of given curves and can be now analyzed using Shape PCA.

Apart from the wearable metrics, several other clinical measures were collected. The description of these measures is given in Table 3.2.

---

[1] https://github.com/jdtuck/fdasrsf_python

Table 3.2: Description of clinical measures against which we correlate our wearable features

Clinical Measures	**Description**
Brooke score	The Brooke Upper Extremity Scale is a 6-point scale that allows classification of upper extremity function and also helps document progression. Points 1-6 are assigned based on functional ability of the patient where higher score indicates more impairment [8].
Cross Sectional Area (CSA (cm^2))	This term is used in the context of anatomy and physiology to describe the size of a muscle. A larger cross-sectional area generally means more muscle fibers, which translates to more force-generating capacity [27].
Normalized Elbow Torque (NET (Nm/cm))	Torque normalized by forearm length.
Average Echogenicity (Avg_Echo (gsv))	Muscle echogenicity refers to the muscle's ability to reflect ultrasound waves, as measured with ultrasound imaging. In SMA, motor neurons in the spinal cord degenerate and die, leading to increased echogenicity of the muscles as the muscle fibers are replaced with fibrous tissue and fat [28]. In DMD, a mutation in the dystrophin gene leads to progressive muscle weakness, degeneration and increased echogenicity due to fat [29].

3.2.3 Statistical Analyses

In order to get more robust results from Shape PCA and also handle multiple visits of participants, we run Shape PCA 100 times with random visit taken for each subject. Then we flip the sign of Singular Value Decomposition (SVD) to get the principal components to be sign aligned with the components of first trial. Then a mean PC score is computed across these runs. All boxplots in Figure 3.7 and correlations in Figure 3.8 are based on this mean

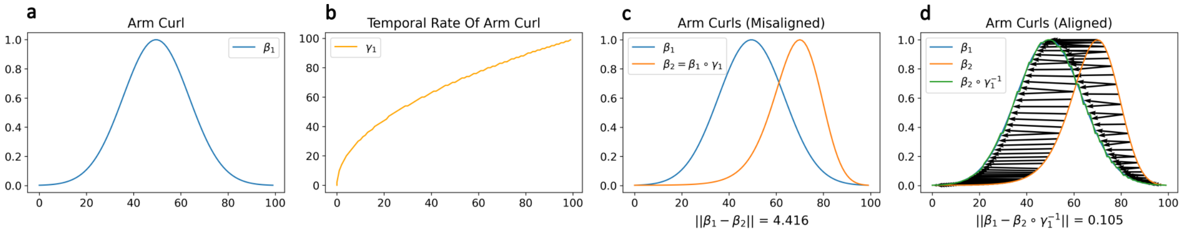

Figure 3.4: A simulated illustration of alignment of arm curls. (a) An example of arm curl. (b) Temporal rate or warping function of this arm curl. (c) An example of misaligned arm curls. (d) Functions after alignment.

PC score.

To gauge the variability in the relationship between wearable modes and clinical variables, we utilized bootstrapping. Figure 3.9 (first column) illustrates the distribution of canonical correlations derived from 10000 bootstrap replicates. In each replicate, we randomly sampled participants with replacement to form a new training set (70% of the data), while the remaining 30% served as a hold-out test set. PLS was fitted on the resampled training data, and its performance, measured by canonical correlation, was assessed on the corresponding test set. This approach captures the uncertainty in estimated relationships due to sampling variability. All the correlations were measured using Pearson correlation coefficient.

For the mixed linear model regression, the random effects accounted for variation in intercepts across different participants (Participant ID), while the fixed effects included the effects of age, cohort, and their interaction. In this analysis, the p-values were calculated using two-sided Wald tests [30]. The significance level was set at $\alpha = 0.01$, and significance was achieved when the interaction effects were statistically different from zero, indicating a significant influence of these interactions on the dependent variable. Additionally, p-values were adjusted for multiple comparisons using the Benjamini-Hochberg method [31]. Shape PCA, PLS, and mixed linear model regression were performed using the FDASRSF [26], Scikit-learn [32], and statsmodels [33] packages, respectively. All other analyses were conducted using Python 3.11.

3.3 Results

3.3.1 Overview of the Approach

Figure 3.1 presents a comprehensive workflow for analyzing Activities of Daily Life (ADL) using sensor-based data and various measurement techniques. Initially, raw sensor signals

(X) are collected during ADL tasks. These signals are then aligned or registered using phase amplitude separation and subjected to Shape-based Principal Component Analysis (PCA) in the shape space. The scores from this shape space are analyzed using Partial Least Squares (PLS) analysis to explore the covariation between the sensor signals (X) and multiple outcome measures (Y), including ultrasound measures (Cross Sectional Area, Average Echogenicity), dynamometer measures (Normalized Elbow Torque), and Brooke scores. The aim is to understand the relationships and potential predictive power of sensor data concerning these outcome measures, despite the absence of a gold standard for Y.

3.3.2 Insights from Curve Registration

To illustrate phase amplitude separation with an example, we initially generate data with a symmetric shape and purely amplitude variation (Figure 3.2a). To demonstrate phase variability, we generate several temporal warping functions (Figure 3.2b). These warping functions indicate the rate at which a motion is performed (slower or faster). Combining the amplitude variation with these warping functions results in both phase and amplitude variation (Figure 3.2c). Attempting to compute the mean of these functions yields the red curve, which is asymmetric (Figure 3.2f), despite the original shapes being symmetric. However, performing phase amplitude separation separates the horizontal variation from the vertical one. This process temporally aligns the functions (Figure 3.2d), recovers the warping functions (Figure 3.2e), and a mean shape (depicted in blue) that is symmetric (Figure 3.2f), providing a much more accurate representation of the original shape.

In Figure 3.3, we present the results of phase-amplitude separation applied to arm curl trajectories from two groups: healthy participants in the top left plot (Figure 3.3a) and participants with DMD/SMA in the plot below (Figure 3.3e). The raw trajectories, particularly from the healthy cohort, exhibit significant phase variability, where similar shapes occur at different times across different trajectories. Phase-amplitude separation is applied specifically to the healthy trajectories, aligning these functions temporally and deriving a mean shape. The resulting elastic mean shape of healthy arm curls is depicted in the third plot (Figure 3.3c), accompanied by the corresponding temporal warping functions shown in the second plot (Figure 3.3b). These warping functions illustrate the variability in phase alignment across different trajectories within the healthy group. From the top right plot (Figure 3.3d), we observe that the peaks and valleys of the healthy trajectories align closely with the healthy mean shape, indicating effective alignment.

In the second row of Figure 3.3, we depict the trajectories from participants with DMD/SMA (Figure 3.3e). Applying phase amplitude separation within this group, we compute the mean shape of DMD/SMA, shown in Figure 3.3g. In Figure 3.3h, we align the DMD/SMA trajectories not to their own mean but to the mean shape derived from healthy participants. This approach aims to highlight deviations from the healthy mean shape. Here, we observe a notable disparity between the peaks and valleys of the DMD/SMA cohort and the healthy mean. As depicted visually in Figure 3.3f, the DMD/SMA trajectories require substantial warping to align them with healthy mean, indicating greater shape variability compared to the healthy trajectories.

3.3.3 Discovering Modes of Variation in Trajectories

In Figures 3.5a-c, we conducted Shape Principal Component Analysis on arm curl trajectories across all cohorts to identify key patterns of variation. The first principal component (VPC1, Figure 3.5a) primarily reflects changes in angular speed while maintaining consistent curl shape. Starting from the mean shape (μ, depicted in black), moving one standard deviation along the positive direction of VPC1 ($\mu + 1\sigma v$, shown in red) reveals a reduction in angular velocity, as observed in the initial plot. This pattern explains 51.78% of the variance across all participants.

The second mode of variation (VPC2, Figure 3.5b) illustrates asymmetry in the motion.

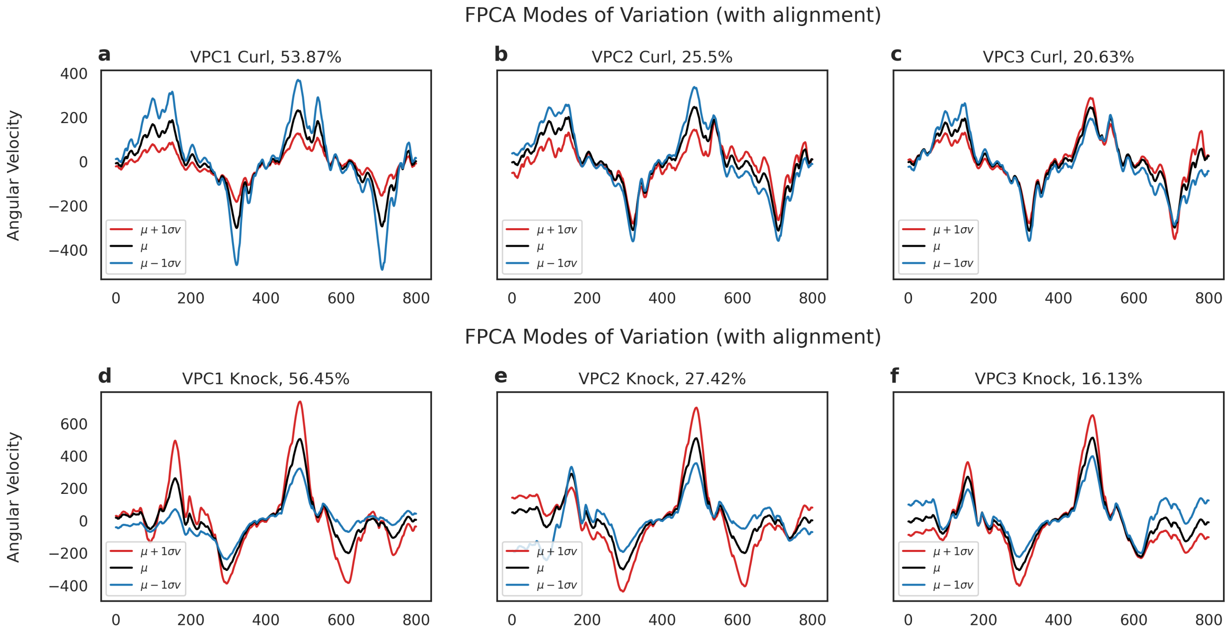

Figure 3.5: (a-c) Vertical modes of variation obtained from Shape PCA on the curl data. (a) The first mode represents scaling, (b) the second asymmetry in motion while (c) the last represents noise. (d-f) Modes of variation obtained from knocking data. (d) The first mode represents scaling. (e) The second mode represents asymmetry in motion while (f) the last represents sensor noise.

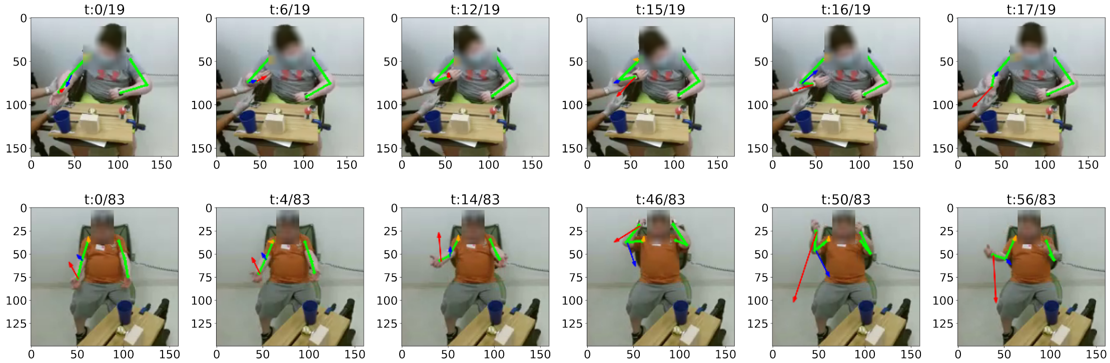

Figure 3.6: Interpretation of Vertical Principal Component 2 of arm curl (VPC2 Curl) in videos of 2 participants. The participants do the downward motion of the arm curl faster than the upward motion, possibly because of some sort of compensation.

Starting from the mean shape (μ, depicted in black), progressing one standard deviation along the positive direction of VPC2 ($\mu + 1\sigma v$, shown in red) reveals a decrease in the height of the peak of the curl while the trough remains unchanged. To validate this observation, we examine joint velocity vectors obtained from Openpose for two participants (Figure 3.6). This analysis indicates that these participants face difficulty during the upward motion phase, while the downward phase occurs more quickly, possibly influenced by gravitational effects. The third mode of variation (VPC3, Figure 3.5c) captures variability in the trajectory's tail. This mode likely reflects sensor noise or temporal segmentation noise.

The second row (Figure 3.5d-f) displays the results of Shape PCA applied to knocking motion curves. Similar patterns to those observed previously emerge. VPC1 appears to represent scaling (Figure 3.5d), indicating variations in the speed of the knocking motion. On the other hand, VPC2 seems to capture asymmetry (Figure 3.5e) between first and second knocking motion. Finally, VPC3 reflects some form of sensor noise (Figure 3.5f). We also conducted Shape PCA on additional activities such as moving a paddle and twisting a door knob. However, these experiments yielded less interpretable results, with principal components showing less structured patterns. Consequently, we focus exclusively on two actions going forward: arm curls and knocking motion.

3.3.4 Analyzing Cohort Differences

In Figure 3.7, we analyze differences in wearable features (X) and clinical measures (Y) among three cohorts. Boxplots are shown for several variables: Age, Brooke score, Average Echogenicity (indicating fat infiltration into tissue), and Normalized Elbow Torque (a normalized measure of strength across age ranges). Additionally, we present projections on the four modes of variation: VPC1 and VPC2 obtained from arm curl and knocking motions. Both DMD and SMA cohorts exhibit higher Average Echogenicity (Figure 3.7c) compared to Healthy, indicating greater fat infiltration into tissue. Consequently, they also show lower

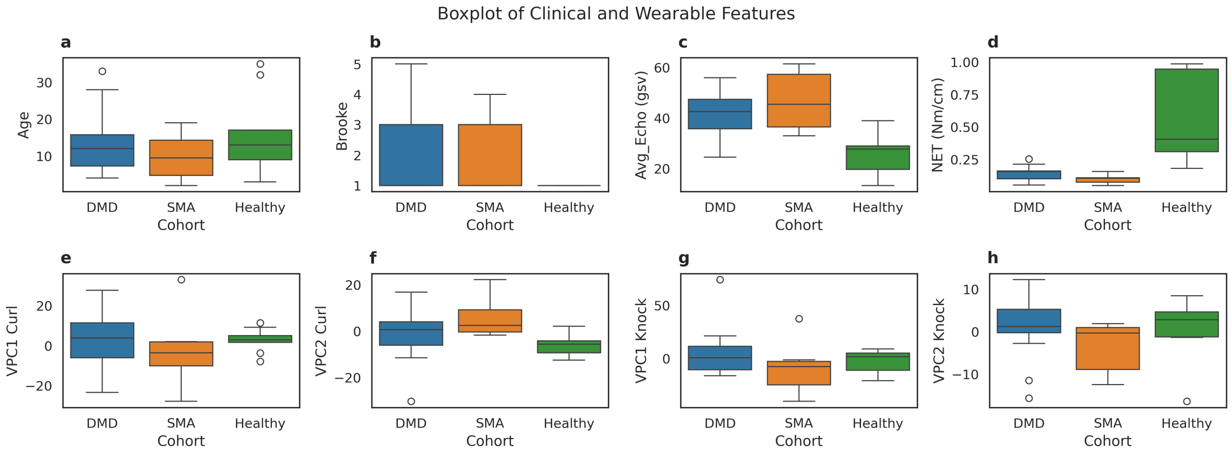

Figure 3.7: Boxplots of some demographic variables along with important clinical measures and feature dimensions. (a) Age, (b) Brooke score, (c) Average Echogenicity (Avg_Echo (gsv)), (d) Normalized Elbow Torque (NET (Nm/cm)), (e) VPC1 Curl (Speed), (f) VPC2 Curl (Asymmetry), (g) VPC1 Knock (Speed), and (h) VPC2 Knock (Asymmetry).

Normalized Elbow Torque (Figure 3.7d), suggesting reduced strength. In the second row (Figure 3.7e-h), we display boxplots of wearable features. VPC1 Curl (Figure 3.7e), representing angular speed in arm curl motion, does not significantly differ between cohorts. Both DMD and SMA show large variations, with functionality ranging similar to Healthy levels. Furthermore, both DMD and SMA cohorts demonstrate lower speed in knocking motion compared to Healthy (Figure 3.7g). Notably, VPC2 Curl activation (Figure 3.7f), which indicates motion asymmetry, is more pronounced in SMA compared to DMD and Healthy. This finding is intriguing given the biological differences between DMD, which involves progressive muscle fiber deterioration due to dystrophin deficiency and SMA, which affects spinal motor neurons. It suggests that SMA may impair subtle motion control, resulting in asymmetries in motion patterns.

3.3.5 Insights from Cross Correlation

In Figure 3.8, we examine the correlations of modes of variation obtained from each activity with the clinical measures described in Table 3.2. In the top row (Figure 3.8a), we observe

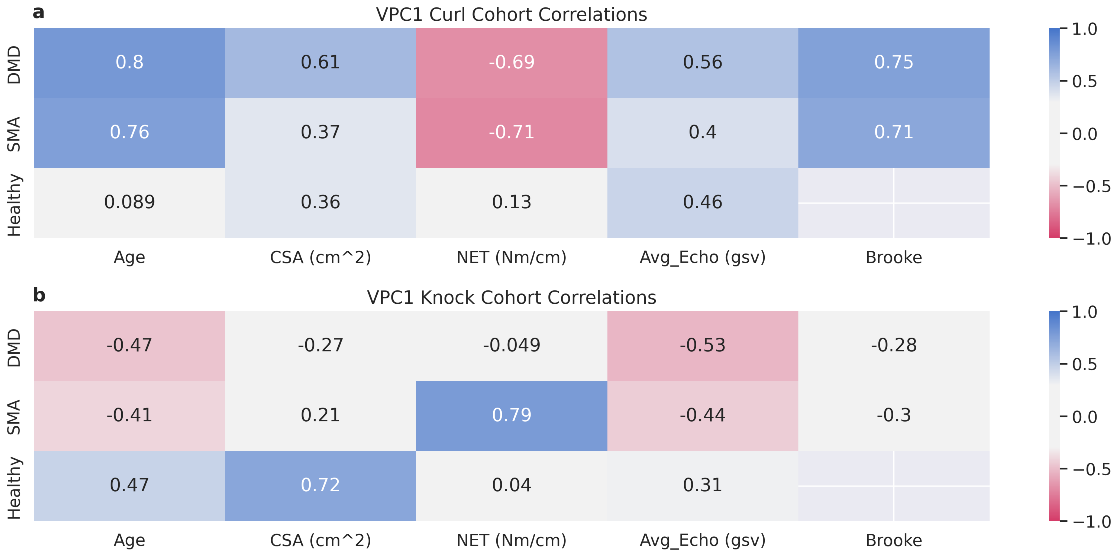

Figure 3.8: Pearson Cross Correlation of different VPC modes with clinical measures for DMD (N=15), SMA (N=7), and Healthy (N=9). (a) Cross correlations for VPC1 Curl (Speed), and (b) VPC1 Knock (Speed).

stronger correlations between VPC1 and age for DMD and SMA compared to the Healthy cohort. This positive correlation suggests that as age increases, VPC1 also increases, indicating a reduction in angular speed. This stronger correlation in DMD and SMA may be due to the progressive nature of these diseases affecting both patient groups. An increase in VPC1 correlates with a decrease in dimensions of strength, as seen in the Normalized Elbow Torque. Additionally, VPC1 for DMD shows a positive correlation with echogenicity, which aligns with increased fat infiltration in muscle fibers, leading to tissue weakening. In both DMD and SMA, VPC1 is positively correlated with the Brooke score, where higher scores indicate poorer muscle function. No correlation with Healthy is shown since Brooke was only collected for patient cohorts. In the second row, VPC1 Knock (Figure 3.8b), representing scaling in knocking motion, displays a similar pattern of correlations, albeit weaker. Since the direction of VPC1 Knock is reversed (moving one standard deviation to the right of the mean implies an increase in speed), its correlations have opposite signs compared to VPC1 Curl.

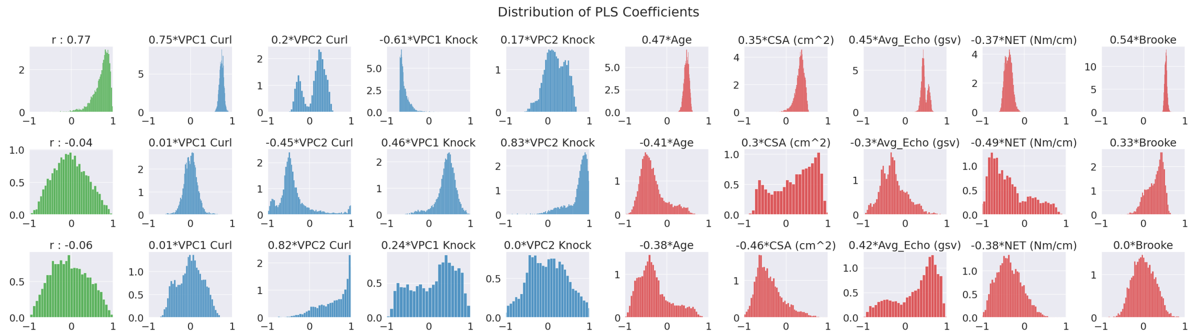

Figure 3.9: Distribution of three different principal PLS correlations (first column) and components. For first principal component, our motor function index has median correlation of $r = 0.77$ (95% CI [0.34, 0.94]) with dimensions of muscle fat infiltration (Avg_Echo), Brooke score, and Age related degenerative changes. Speed of curl (VPC1 Curl) and knock (VPC1 Knock) have tighter spread in distribution than the asymmetry features (VPC2 Curl and VPC2 Knock).

3.3.6 Combining Modes of Variation

To develop a comprehensive index for assessing function in DMD and SMA cohorts (Healthy was omitted due to missing Brooke), we employed Partial Least Squares (PLS) to combine projections atop the principal component dimensions and correlate them with clinical variables. To gauge the variability in the relationship between wearable modes and clinical variables, we utilized bootstrapping. Figure 3.9 (first column) illustrates the distribution of canonical correlations derived from 10000 bootstrap replicates. As shown in the first row of Figure 3.9, our primary canonical dimension ($0.75 \times \text{speed curl} - 0.61 \times \text{speed knock} + 0.2 \times \text{asymmetry curl} + 0.17 \times \text{asymmetry knock}$) achieved a median canonical correlation of $r = 0.77$, with a 95% confidence interval of [0.34, 0.94] across the 10000 bootstrapped test sets. This indicates a robust association between this linear combination of wearable features and dimensions such as muscle fat infiltration (Avg_Echo), Brooke score, and age-related degenerative changes. The narrower spread of coefficients for speed of motion (VPC1 Curl and VPC1 Knock) underscores their particular significance within this dimension. Following them are asymmetry in curl motion (VPC2 Curl) and asymmetry in knocking motion (VPC2 Knock). Given the lower correlations and higher variance in coefficient estimates observed in

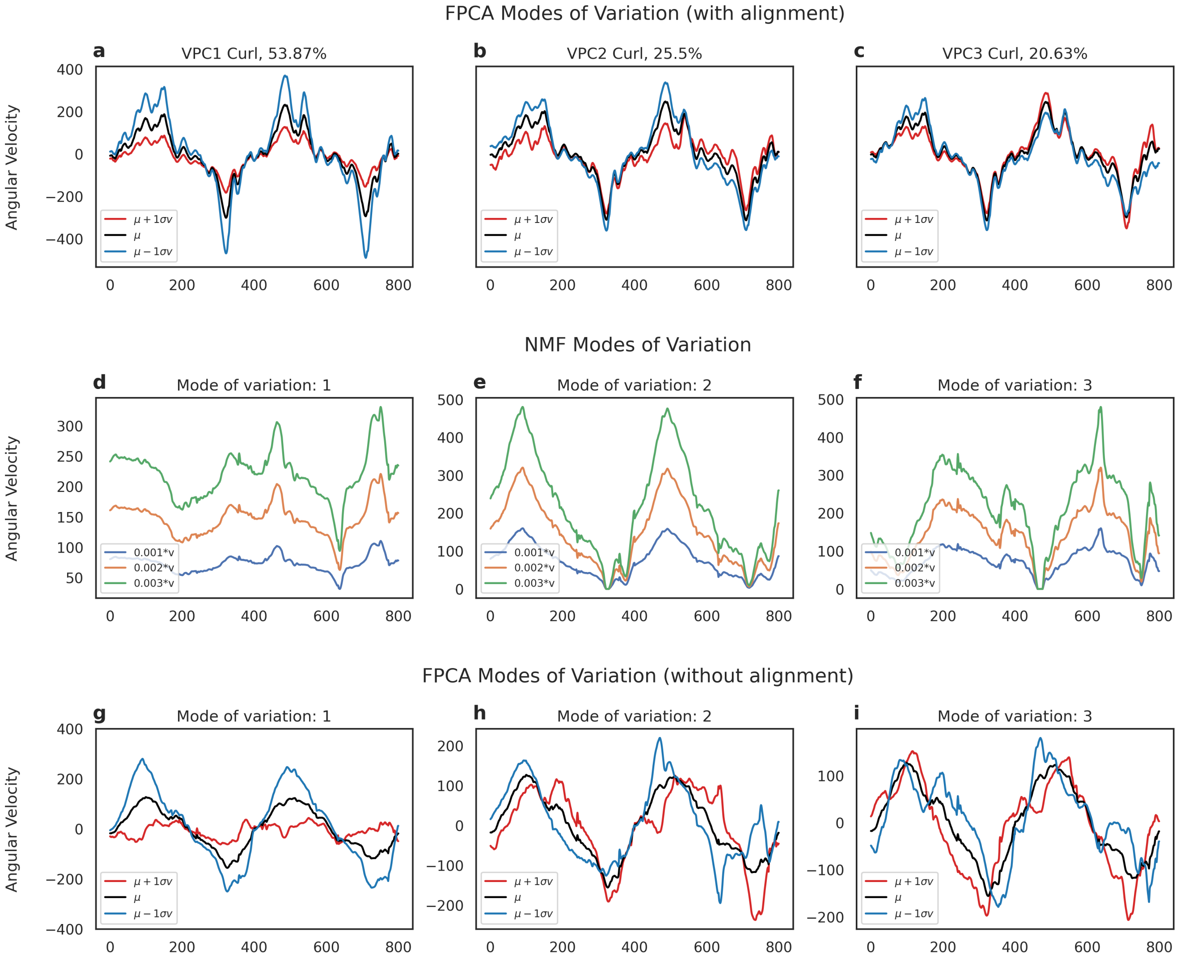

Figure 3.10: Comparison of different decomposition methods, (a-c) Shape PCA with alignment leads to much more interpretable modes of variation than (d-f) NMF, and (g-i) Functional PCA without alignment because of the phase variability.

the second and third modes ($r = -0.04$ and $r = -0.06$, respectively), we opted for the first canonical dimension as our motor function index. This decision was guided by its stronger bootstrapped correlation and more stable coefficient estimates.

3.3.7 Comparison with other Decomposition Techniques

We compared our algorithm with other low-rank decomposition techniques: specifically, Functional PCA without phase-amplitude separation and Non-negative Matrix Factorization (NMF). The modes of variation obtained from each technique are illustrated in Figure

Table 3.3: Performance comparison for different algorithms reported in terms of bootstraped canonical correlation of each component

Algorithm	Component	Median (50th percentile)	[5-95]% Percentile
Shape PCA (Aligned)	1	0.77	[0.34, 0.94]
NMF (No alignment)	1	0.63	[0.01, 0.94]
Functional PCA (No alignment)	1	0.36	[-0.3, 0.81]
Shape PCA (Aligned)	2	-0.04	[-0.66, 0.66]
NMF (No alignment)	2	0.28	[-0.47, 0.81]
Functional PCA (No alignment)	2	0.18	[-0.60, 0.85]
Shape PCA (Aligned)	3	-0.06	[-0.72, 0.71]
NMF (No alignment)	3	0.14	[-0.59, 0.77]
Functional PCA (No alignment)	3	-0.01	[-0.67, 0.69]

3.10, and the corresponding canonical correlations are summarized in Table 4.2. Our framework achieves a higher median canonical correlation and a narrower confidence interval for the first component.

3.3.8 Mixed-Effects Regression

In Table 3.4, we examined the relationship between age and speed of movement in DMD, SMA, and Healthy control groups. We conducted mixed-effects regression, modeling VPC1 Curl as an interaction between age and cohort. The results reveal significant associations between VPC1 Curl and both age and cohort status. Age significantly influenced VPC1 Curl within each cohort, with older participants generally demonstrating higher values of VPC1 Curl. Specifically, for DMD ($\beta = 1.337$, corrected $p = 0.001$) and SMA ($\beta = 2.530$, corrected $p = 0.002$) cohorts, the positive coefficients indicate an age-related decline in speed of curl, suggesting a loss of ability. Conversely, the Healthy cohort did not show a significant temporal trend. The intercept term for individuals with DMD and SMA showed negative values, suggesting initially higher motion speeds. This finding might be attributed to the presence of higher-functioning individuals within these cohorts who initially exhibit function comparable to or better than Healthy controls but experience a decline over time,

Table 3.4: Mixed Linear Model Regression: VPC1 Curl ∼ Age * Cohort

	Coef.(β)	Std.Err.	z	corrected $p>$ |z|	[0.025	0.975]
Intercept:Cohort[T.Healthy]	1.937	6.205	0.312	0.90588	-10.224	14.098
Intercept:Cohort[T.DMD]	-18.864	7.667	-2.461	0.03329	-33.891	-3.838
Intercept:Cohort[T.SMA]	-31.125	9.341	-3.332	**0.00258**	-49.432	-12.817
Age:Cohort[T.Healthy]	0.047	0.336	0.141	0.95578	-0.611	0.706
Age:Cohort[T.DMD]	1.337	0.361	3.706	**0.00126**	0.630	2.044
Age:Cohort[T.SMA]	2.530	0.728	3.477	**0.00202**	1.104	3.957
Group Var	54.213					

Table 3.5: Mixed Linear Model Regression: VPC2 Curl ∼ Age * Cohort

	Coef.(β)	Std.Err.	z	corrected $p>$ |z|	[0.025	0.975]
Intercept:Cohort[T.Healthy]	-1.769	5.223	-0.339	0.90588	-12.005	8.468
Intercept:Cohort[T.DMD]	0.374	6.746	0.055	0.95578	-12.847	13.595
Intercept:Cohort[T.SMA]	13.064	3.053	4.279	**0.00023**	7.080	19.047
Age:Cohort[T.Healthy]	-0.258	0.264	-0.976	0.49331	-0.776	0.260
Age:Cohort[T.DMD]	0.451	0.389	1.158	0.49331	-0.312	1.213
Age:Cohort[T.SMA]	-0.442	0.446	-0.992	0.49331	-1.316	0.431
Group Var	58.170					

as indicated by the slope terms.

In Table 3.5, we examined the relationship between age and asymmetry of movement in DMD, SMA, and Healthy control groups. We conducted mixed-effects regression, modeling VPC2 Curl as an interaction between age and cohort. The regression analysis reveals a significantly greater intercept of SMA cohort on asymmetry of movement ($\beta = 13.064$, corrected $p = 0.00023$), indicating a notable asymmetry among SMA patients. The corrected p-value still indicates a significant result, reinforcing the observation of increased asymmetry in the SMA cohort.

3.4 Discussion and Future Work

Our approach holds significant promise in clinical practice and research for several reasons. Firstly, by leveraging shape analysis of motion trajectories captured by wearable sensors, we extract rich, quantitative data that traditional clinical assessments may overlook. This provides a more comprehensive understanding of motor function in children with neuromuscular disorders, enabling tailored interventions and therapies. The use of Shape Principal Component Analysis allows us to identify nuanced patterns in movement, such as scaling and asymmetry, across various daily activities. These insights are crucial for clinicians to assess functional limitations and track changes over time more accurately than conventional methods permit.

Moreover, the Partial Least Squares (PLS) technique uncovers a covariation mode that correlates significantly with clinical measures like muscle fat infiltration, strength assessments, motor function indices, and age. This PLS-derived mode serves as an interpretable index of motor function, offering transparency and clinical relevance, which contrasts with the black-box nature of many current movement analysis tools. Practically, our method supports the development of home-based monitoring systems. These systems can continuously collect data over extended periods, reducing the necessity for frequent clinic visits and enhancing patient convenience. This longitudinal data collection not only facilitates early detection of subtle functional changes but also empowers caregivers to report on daily function more comprehensively.

Furthermore, integrating activity recognition algorithms into these systems will enhance their utility by providing detailed insights into how children perform activities of daily living. This holistic approach paints a clearer picture of functional capabilities, aiding clinicians in making informed decisions about treatment adjustments and interventions. The non-intrusive nature of wearable sensors is particularly advantageous for monitoring disease progression, especially in patients undergoing novel therapies such as gene therapy. By minimizing the need for physical visits, telemedicine supported by wearable sensors extends clinical care to remote areas and during public health emergencies, ensuring continuity of care and improving patient outcomes.

In conclusion, our methodological approach not only advances the field of movement analysis in neuromuscular disorders but also promises practical applications in enhancing patient monitoring, clinical decision-making, and therapeutic outcomes. Future research efforts will focus on expanding participant cohorts, validating our findings across diverse populations, and refining our approach to accommodate varying clinical contexts and needs.

Chapter 4

Jointly Analyzing Emg and Motion Shapes for Understanding Motor Function Rehabilitation in Stroke

4.1 Introduction

Stroke affects more than 795,000 patients per year. To understand post rehabilitation function in stroke patients, it's crucial to analyze both motion and muscle activity, encompassing both "form" and "function". Relying on a single modality is insufficient for a comprehensive assessment. For example, consider a stroke patient with good kinematic data but poor EMG activity. This patient might exhibit smooth and efficient walking patterns, suggesting good functional recovery. However, the EMG data could reveal underlying neurochemical deficiencies or abnormal muscle activation patterns that aren't apparent through kinematic analysis alone. Conversely, another stroke patient might have poor kinematic data but good EMG activity. This patient could show irregular, spastic gait patterns, indicating poor functional recovery. Nonetheless, the EMG data might demonstrate strong and normal muscle activation, suggesting that the muscles themselves are functioning well but the control and coordination aspects are impaired. Therefore, a joint analysis of both kinematic and EMG data provides deeper insights into the patient's condition, revealing nuances that might be missed when focusing on only one modality.

Several studies have focused on analyzing stroke kinematic data ([1]). A common choice of study design is to allow participants to perform the motion naturally, to not constrain their motion. However this can lead to phase variability in the dataset, since different patients might perform the motion at different speeds. Furthermore, since the setup does not involve a treadmill, there can be translation/rotation variability where same motion shapes with different starting configurations relative to camera can have different sensor signals. Finally, variation in participant sizes can cause kinematic patterns with same shapes to have different norm of signals.

Similarly, emg data also suffers from phase variability depending on walking speed of the participant. An example of this is shown in Figure 1, first column, where despite the kinematic and emg signals being generate by a periodic walking pattern, it's hard to see any periodic structure in the raw data. The presence of rotation/translation/scale/phase variability in kinematic and phase variability in emg make it challenging to see any periodic structure in the raw data.

In our current work, we use techniques from statistical shape analysis to the problem of identifying differences between hemiplegic vs normal gaits based on jointly registering both kinematic and emg modalities. In particular, we focus on the following research questions:

Given we have freeform kinematic data with phase/scale/rotation/translation variability X_{kin}, EMG data with phase variability X_{emg}.

1. How do we perform registration of such complex biomechanical data to eliminate nuisance variables like rotations and temporal rates of actions?

2. How do we summarize the high dimensional biomechanical data to useful and parsimonious modes of variation?

4.2 Related Work

There is a rich body of literature on using Dynamic Time Warping in the context of stroke. [34] used a real-time variant of the dynamic time warping (DTW) algorithm for motor exercise recognition, particularly in the context of neurological rehabilitation. The algorithm provides real-time feedback to neurological patients during motor rehabilitation sessions. [35] investigated the effectiveness of dynamic time warping (DTW) in analyzing gait pattern similarity, aiming to address a gap in its application within gait research. [36] used DTW distance to objectively measure upper limb mobility post-stroke. They found a reference signal by averaging motion samples collected from rehabilitation experts and determined the DTW distance between this reference motion and stroke patient's motion. Several other works have focused on using Dynamic Time Warping [36, 37, 38, 39], removing rotation, translation, and scaling variability has received less attention. Some approaches have focused on combining DTW with rotations, but this approach faces challenges when performing PCA with the data because DTW is not a proper metric distance. Rotational data lies on non-Euclidean manifolds, where the absence of a global vector space makes it challenging to extend the notion of PCA. A recent line of work [4, 40] has tried to address this by performing PCA in the tangent space of manifolds. We extend this approach in our paper.

4.3 Methodology

4.3.1 Kendall Shape Space based transported srvf formulation

Given kinematic data, we represent each skeleton frame as a matrix of k landmarks storying $m = 3$ xyz coordinates of each joint in the body. We consider the space of $m \times k$ matrices representing our k landmarks.

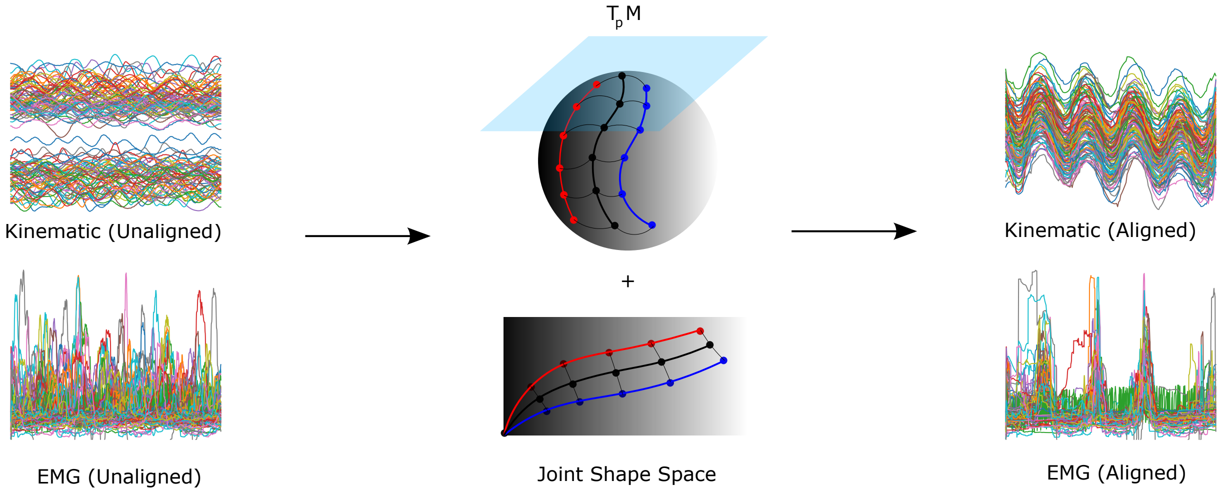

Figure 4.1: a) Action of nuisance groups (rotation/translation/scaling/reparameterizations) obfuscates the latent periodic structure in the data and makes it challenging to perform simple tasks like computing means. b) Registering raw data with our method allows us to see this structure as well as analyze both kinematic and muscle activity shapes.

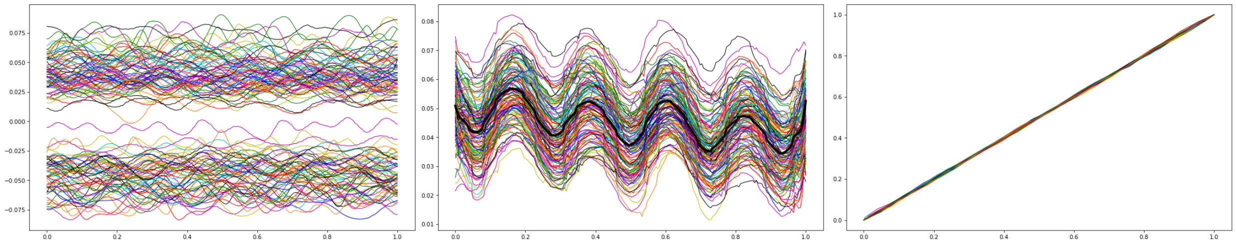

Figure 4.2: Example of kinematic registration.

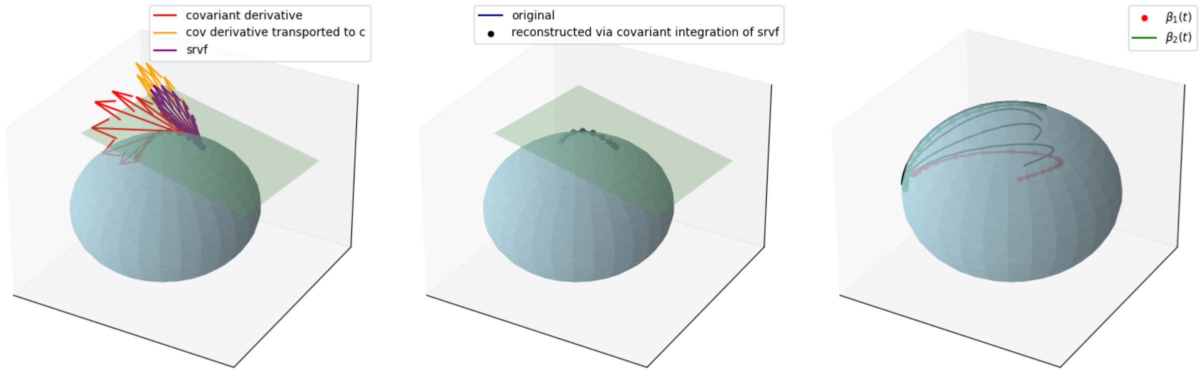

Figure 4.3: Example of tsrvf construction and trajectory interpolation on a Sphere Manifold.

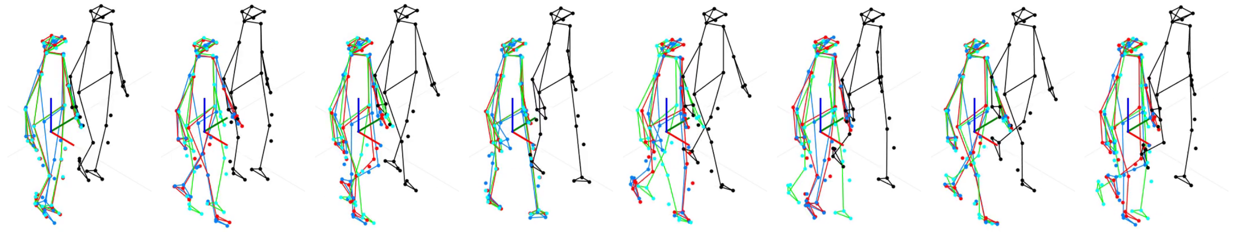

Figure 4.4: Comparison of registration with [41].

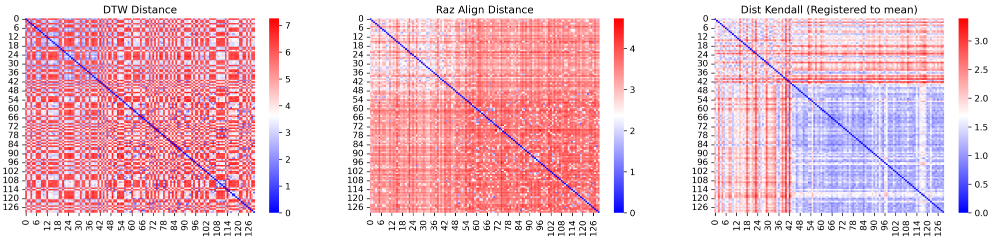

Figure 4.5: Pairwise distances, block structure in healthy possibly because easier to register healthy to another healthy. Middle is registration from [41].

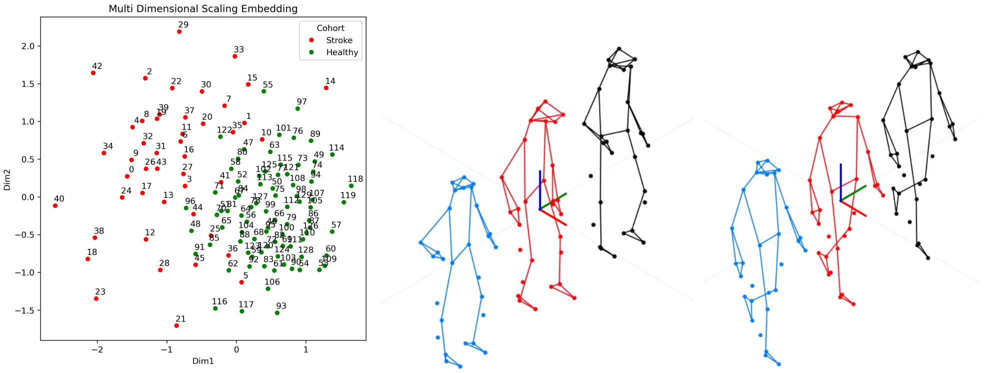

Figure 4.6: 14, 10, 36 are stroke patients close to healthy, 42, 34, 2 are stroke patients far from healthy.

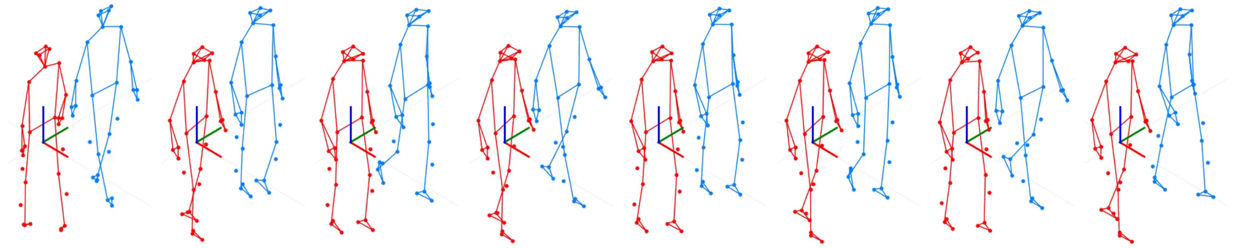

Figure 4.7: Mean calculation from registered curves. Stroke mean shown in red while healthy shown in blue. Hemiplegic show dragging.

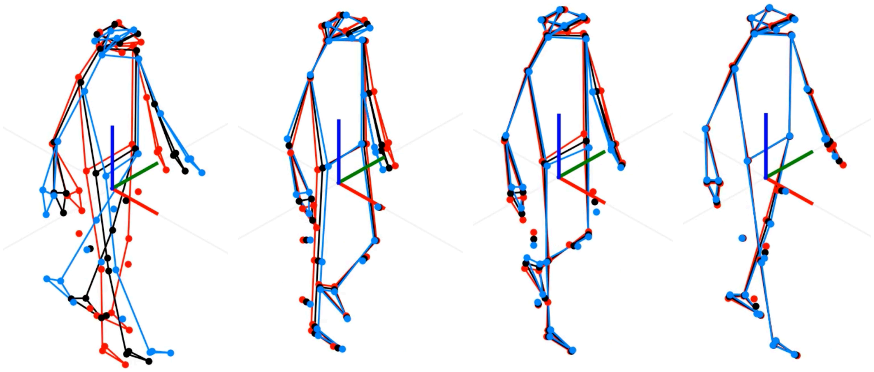

Figure 4.8: Pca modes 1 (short stride + stiffer limbs + head position up or down),7 (left arm variability), 9 (elbow variation), 14 (Right Shoulder variation). 7, 9 and 14 seem to capture differences between stroke left and right

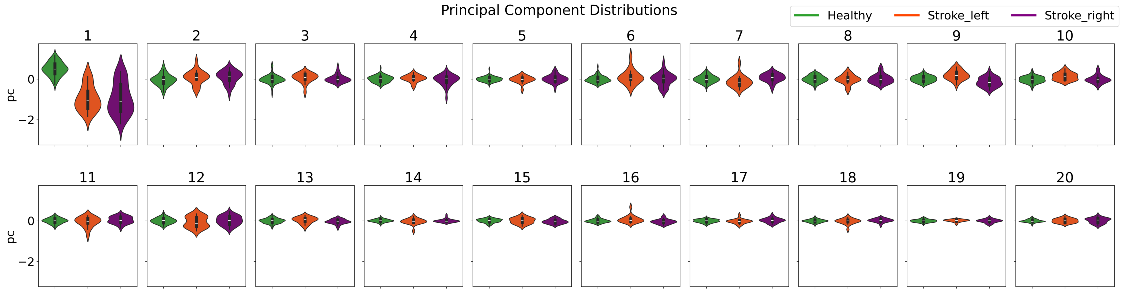

Figure 4.9: Boxplots showing separation between healthy and stroke via pcs

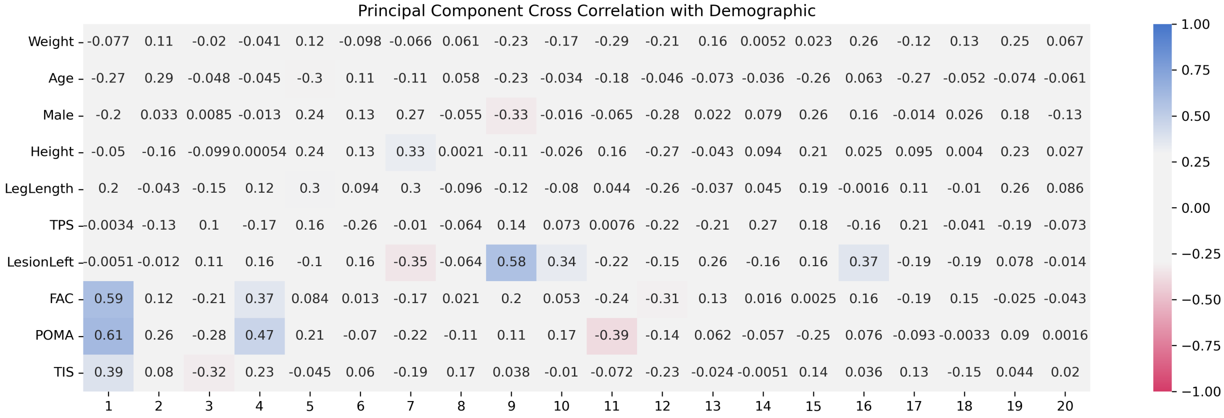

	1	2	3	4	5	6	7	8	9	10	11	12	13	14	15	16	17	18	19	20
Weight	-0.077	0.11	-0.02	-0.041	0.12	-0.098	-0.066	0.061	-0.23	-0.17	-0.29	-0.21	0.16	0.0052	0.023	0.26	-0.12	0.13	0.25	0.067
Age	-0.27	0.29	-0.048	-0.045	-0.3	0.11	-0.11	0.058	-0.23	-0.034	-0.18	-0.046	-0.073	-0.036	-0.26	0.063	-0.27	-0.052	-0.074	-0.061
Male	-0.2	0.033	0.0085	-0.013	0.24	0.13	0.27	-0.055	-0.33	-0.016	-0.065	-0.28	0.022	0.079	0.26	0.16	-0.014	0.026	0.18	-0.13
Height	-0.05	-0.16	-0.099	0.00054	0.24	0.13	0.33	0.0021	-0.11	-0.026	0.16	-0.27	-0.043	0.094	0.21	0.025	0.095	0.004	0.23	0.027
LegLength	0.2	-0.043	-0.15	0.12	0.3	0.094	0.3	-0.096	-0.12	-0.08	0.044	-0.26	-0.037	0.045	0.19	-0.0016	0.11	-0.01	0.26	0.086
TPS	-0.0034	-0.13	0.1	-0.17	0.16	-0.26	-0.01	-0.064	0.14	0.073	0.0076	-0.22	-0.21	0.27	0.18	-0.16	0.21	-0.041	-0.19	-0.073
LesionLeft	-0.0051	-0.012	0.11	0.16	-0.1	0.16	-0.35	-0.064	0.58	0.34	-0.22	-0.15	0.26	-0.16	0.16	0.37	-0.19	-0.19	0.078	-0.014
FAC	0.59	0.12	-0.21	0.37	0.084	0.013	-0.17	0.021	0.2	0.053	-0.24	-0.31	0.13	0.016	0.0025	0.16	-0.19	0.15	-0.025	-0.043
POMA	0.61	0.26	-0.28	0.47	0.21	-0.07	-0.22	-0.11	0.11	0.17	-0.39	-0.14	0.062	-0.057	-0.25	0.076	-0.093	-0.0033	0.09	0.0016
TIS	0.39	0.08	-0.32	0.23	-0.045	0.06	-0.19	0.17	0.038	-0.01	-0.072	-0.23	-0.024	-0.0051	0.14	0.036	0.13	-0.15	0.044	0.02

Figure 4.10: Correlation of demographic with pcs

$$X \epsilon \mathbb{R}^{m \times k} \tag{4.1}$$

These matrices are acted upon by the group of translations, scaling and rotations. In order to compute shape distance between skeletons, we need to remove the action of these nuisance groups.

We mean center these matrices to remove translation as a degree of freedom. This yields a new vector space where translation has been quotiented out.

$$V_m^k = \{X \epsilon \mathbb{R}^{m \times k} : \sum_{i=1}^{k} X[:, i] = 0\} \tag{4.2}$$

Scaling is quotiented out by imposing the unit frobenius norm constrain

$$S_m^k = \{X \epsilon V_m^k : \|X\|_2 = 1\} \tag{4.3}$$

.

Because of the unit norm constraints, the preshape space has a spherical geometry.

Since translations and scalings have been quotiented out, our landmark matrices lying in S_m^k are acted upon by a group of rotations.

$$\mathcal{SO}(3) = \{R \in \mathbb{R}^{3 \times 3} \mid R^T R = I, det(R) = 1\} \tag{4.4}$$

.

We define an equivalence relation between two skeletons $X_1, X_2 \epsilon S_m^n$ $X_1 \sim X_2$ if and only if $X_2 = RX_1$

This allows us to define the shape space as a quotient space under this equivalence relation

$$\Sigma_m^k = S_m^n / \sim \tag{4.5}$$

For points away from singularities, the quotient map is a Riemannian Submersion. This allows us to define geodesics and the distance between two shapes $p_1, p_2 \epsilon \Sigma_m^n$ can be defined as

$$d(p_1, p_2) = inf_R d(X_1, R * X_2) \tag{4.6}$$

Where d is the geodesic distance on the sphere. Orthogonal Procrustes Analysis for alignment is used to find the solution to this problem.

TSRVF distance Let $\beta_j^{\text{kin}}(t) : [0,1] \to \Sigma$ represent a collection of kinematic trajectories lying on a manifold Σ, and $\beta_j^{\text{emg}}(t) : [0,1] \to \mathbb{R}^n$ represent a collection of EMG trajectories in Euclidean space. We choose a reference trajectory $c \in \Sigma$.

We first use numerical differentiation to calculate the covariant derivative for each kinematic trajectory and simple differences for each EMG trajectory, followed by the computation of the joint SRVF.

Given a joint SRVF q_j, we can recover the kinematic and EMG trajectories β_j^{kin} and β_j^{emg} via covariant integration with the initial condition starting from reference c.

We perform the mean calculation based on the joint SRVF.

We start by setting $\mu_{\beta^{\text{kin}}} = \beta_1^{\text{kin}}$ and $\mu_{\beta^{\text{emg}}} = \beta_1^{\text{emg}}$.

4.4 Results

In Figure 4.2, first column, we show unregistered kinematic (first landmark, x coordinate) and EMG data across all participants. Due to action of nuisance groups (rotations/translations/scaling/phase in kinematic, phase in EMG), the data shows no periodic structure

Algorithm 1 Covariant Derivative and Transported Joint SRVF Calculation

```
Input: Collection of kinematic trajectories $\{\beta_j^{\text{kin}}(t)\}$, collection of EMG trajectories $\{\beta_j^{\text{emg}}(t)\}$, reference trajectory $c$
for each trajectory $\beta_j^{\text{kin}}(t)$ and $\beta_j^{\text{emg}}(t)$ do
    Calculate $\dot{\beta}_j^{\text{kin}}(t)$ using numerical differentiation:
        $$\dot{\beta}_j^{\text{kin}}(t) \approx \left( \frac{\log_{\beta_j^{\text{kin}}(t)}(\beta_j^{\text{kin}}(t+\Delta t))}{\Delta t} \right)_{\beta_j^{\text{kin}}(t) \to c}$$
    Calculate $\dot{\beta}_j^{\text{emg}}(t)$ via difference:
        $$\dot{\beta}_j^{\text{emg}}(t) \approx \frac{\beta_j^{\text{emg}}(t+\Delta t) - \beta_j^{\text{emg}}(t)}{\Delta t}$$
    Form the joint derivative $\dot{\beta}_j^{\text{joint}}(t)$:
        $$\dot{\beta}_j^{\text{joint}}(t) = \begin{pmatrix} \dot{\beta}_j^{\text{kin}}(t) \\ \dot{\beta}_j^{\text{emg}}(t) \end{pmatrix}$$
    Calculate the joint SRVF $q_j(t)$:
        $$q_j(t) = \left( \frac{\dot{\beta}_j^{\text{joint}}(t)}{\sqrt{\|\dot{\beta}_j^{\text{joint}}(t)\|}} \right)$$
end for
Output: Joint SRVF representations $\{q_j(t)\}$
```

Algorithm 2 Trajectory Recovery

```
Input: Joint SRVF $q_j(t)$, reference trajectory $c$
Initialize $\beta_j^{\text{kin}}(0) = c$
for each time step $t$ do
    Calculate the joint derivative $\dot{\beta}_j^{\text{joint}}(t)$:
        $$\dot{\beta}_j^{\text{joint}}(t) = q_j(t)\|q_j(t)\|$$
    Extract the kinematic and EMG components:
        $$\dot{\beta}_j^{\text{kin}}(t) = \dot{\beta}_j^{\text{joint,kin}}(t)$$
        $$\dot{\beta}_j^{\text{emg}}(t) = \dot{\beta}_j^{\text{joint,emg}}(t)$$
    Update the kinematic trajectory:
        $$\beta_j^{\text{kin}}(t+\Delta t) = \exp_{\beta_j^{\text{kin}}(t)}\left(\dot{\beta}_j^{\text{kin}}(t)_{c\to\beta_j^{\text{kin}}(t)}\Delta t\right)$$
    Update the EMG trajectory:
        $$\beta_j^{\text{emg}}(t+\Delta t) = \beta_j^{\text{emg}}(t) + \dot{\beta}_j^{\text{emg}}(t)\Delta t$$
end for
Output: Recovered kinematic and EMG trajectories $\{\beta_j^{\text{kin}}(t)\}$ and $\{\beta_j^{\text{emg}}(t)\}$
```

Algorithm 3 Mean Calculation

```
Initialize $\mu_{\beta^{\text{kin}}} = \beta_1^{\text{kin}}$ and $\mu_{\beta^{\text{emg}}} = \beta_1^{\text{emg}}$
Calculate initial joint SRVF $\mu_q(t) = \text{tsrvf}(\mu_{\beta^{\text{kin}}}, \mu_{\beta^{\text{emg}}})$
repeat
    for each joint trajectory $\beta_j^{\text{kin}}(t)$ and $\beta_j^{\text{emg}}(t)$ do
        Minimize:
            $$\min_{\gamma_j} \sum \|\mu_q - q_j \circ \gamma_j \sqrt{\dot{\gamma}_j}\|_2^2$$
        Update $\hat{\beta}_j^{\text{kin}}$ and $\hat{\beta}_j^{\text{emg}}$:
            $$\hat{\beta}_j^{\text{kin}} = \beta_j^{\text{kin}} \circ \gamma_j$$
            $$\hat{\beta}_j^{\text{emg}} = \beta_j^{\text{emg}} \circ \gamma_j$$
    end for
    Update $\mu_{\beta^{\text{kin}}}(t)$ and $\mu_{\beta^{\text{emg}}}(t)$:
        $$\mu_{\beta^{\text{kin}}}(t) = \exp\left(\frac{\sum \epsilon \log_{\mu_{\beta^{\text{kin}}}(t)} \hat{\beta}_j^{\text{kin}}(t)}{N}\right)$$
        $$\mu_{\beta^{\text{emg}}}(t) = \frac{\sum \hat{\beta}_j^{\text{emg}}(t)}{N}$$
until convergence
Output: Mean trajectories $\mu_{\beta^{\text{kin}}}(t)$ and $\mu_{\beta^{\text{emg}}}(t)$
```

despite being generated by a periodic gait. We embed the trajectories in joint shape space (middle column), where each trajectory is aligned to its mean shape. This results in a periodic kinematic and EMG trajectory (right column).

In Figure 4.3, We illustrate the transported srvf by first simulate a trajectory on a sphere. We calculate a covariant derivative as described in the methods and then parallel transport the vector field to the tangent space of a reference point **c**. The reconstruction is shown in the middle plot. The last plot shows geodesics between two random trajectories on the sphere.

In Figure 4.4, we compare our results from one of the recent stroke recognition setups proposed in [41]. The original shape is shown in red while the other shape is shown in black. The registration algorithm has to match the black sequence with the red sequence, in order to compare these trajectories. A good registration algorithm will align these two to each other while not deforming the source skeleton sequence too much. We show our TSRVF registration in blue while the registration from [41] is shown in green. As seen here, the registration from [41] often differs in phase compared to the target sequence while our registration matches it quite accurately. This is further quantified in Table 1 where we compare our registration algorithm with previous methods for computing distances/registering stroke biomechanical trajectories.

In Figure 4.5, we compute pairwise distances based on DTW distance (left), distance from [41] (middle), and Kendall shape distance (right). Numbers 0-49 indicate stroke patients while the remaining represent healthy. It's hard to make out any evidence of a cluster from the Euclidean or Procrustes registered distances. However, a clear block is evident from our registration distances. This can be further seen in Figure 4.6 where MDS identifies clear clusters of healthy and stroke patients along with identifying patients with the most extreme gait (14,10, and 36). Compare this to stroke patients with almost healthy gait (42,34, and 2).

In Figure 4.7, we use our registration to compute a mean for both the stroke and healthy cohorts individually. Some clear patterns are visible. The stroke mean has a shorter stride length and reduced knee flexion compared to the healthy patients. They also demonstrate lesser swaying of hands and a bent neck posture.

In order to investigate this further, in Figure 4.8, we use functional principal component analysis on the combined stroke and healthy registered biomechanical trajectories. We plot the mean trajectory in black while deviations of -1 std deviation and +1 std deviation are shown in blue and red. We point out several interesting PC modes while the remaining are shown in the appendix. The first PC mode seems to capture variation in scaling of participants, with the red skeleton showing a shorter stride length, stiffer arm sway, and a neck position which is bent down. As seen from 4.9, this PC mode is especially effective in separating both left and right hemiplegic participants from healthy. As seen from Fig 4.10, this PC mode is also correlated with two of the baseline metrics: The Functional Ambulatory Category (FAC) and the Tinetti Performance Oriented Mobility Assessment (POMA) with a correlation of 0.59 and 0.61 respectively.

PC mode 7 seems to be associated with variability in left arm and trunk rotation while walking. It shows some separation between left and right hemiplegia and has a weak correlation with the Y variable LesionLeft, indicating whether the stroke is on the left or the right side of the body. PC mode 9 is particularly interesting, it's representing some form of elbow variation, shows clear separation between left vs right sided hemiplegia and has a correlation of 0.58 with LesionLeft.

Finally, PC mode 14 seems to represent variation in the right shoulder as seen from the skeletal sequence.

Next, we focus our attention on registration of the EMG. In Figure 11, first two rows, we show raw EMG data processed with a Butterworth filter along with a root mean square transformation on a window of 50ms. The data appears to be really noisy without any

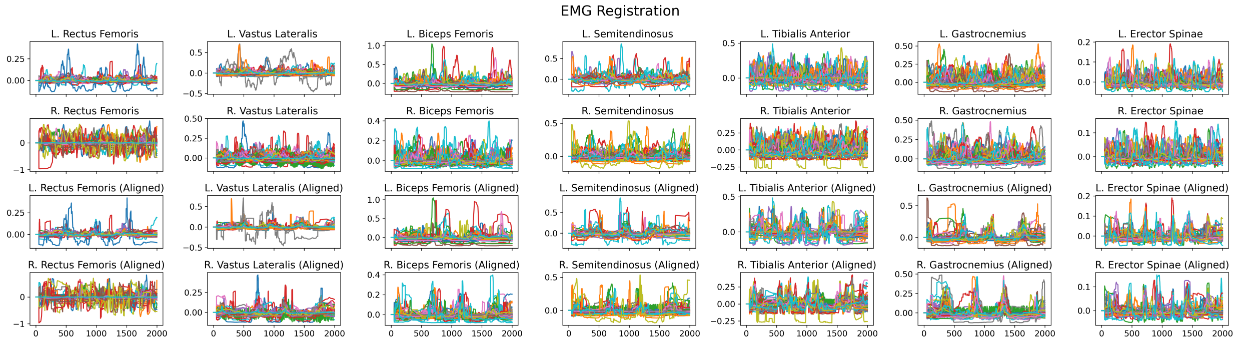

Figure 4.11: EMG Registration

apparent periodic pattern which would indicate it was generated by walking. Next, we run registration with phase variability and align each EMG function to the mean shape. Post-registration, it's a lot easier to see a periodic pattern in several of the muscle signals.

In Figure 12, we show the first PC eigenfunction associated with functional PCA of EMG. This eigenfunction seems to represent a global scaling of periodic activity of all the muscles. Further analysis reveals that this eigenfunction, similar to the first PC kinematic mode, is especially useful in separating hemiplegic from healthy.

In Table 4.1, we show a comparison of our method with some previously published methods in the stroke kinematic quality assessment domain. Functional PCA Kendall outperforms other methods.

In Figure 13, we show F1 scores for classification of Healthy vs Paretic Left vs Paretic Right for all the participants. A and B show the F1 score of kinematic, EMG, and a joint model built on top of the first R functional coefficients from both kinematic and EMG. The unaligned model performs much more poorly compared to the aligned one. In C and D, we show the same plot but here we evaluate the capacity of each PC dimension individually to perform classification. PC modes 1, 7, and 9 seem particularly interesting.

Finally, in Table 4.2, we compare our best performing method for Paretic vs Healthy classification to other models.

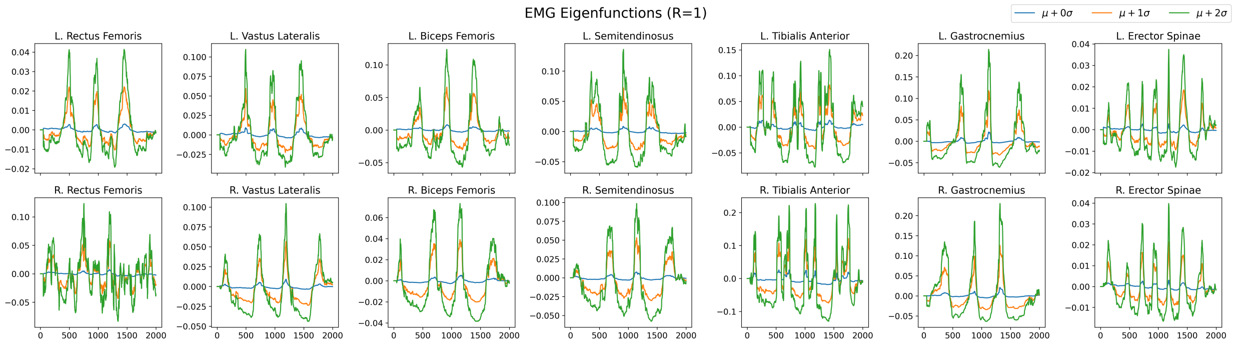

Figure 4.12: First EMG Eigenfunction

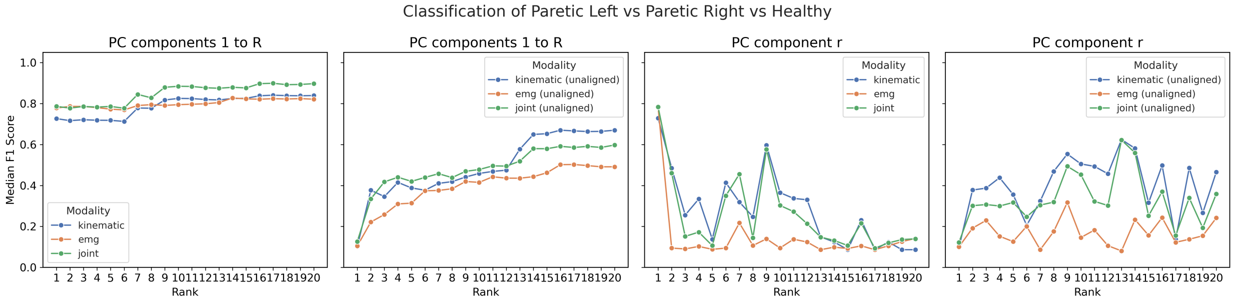

Figure 4.13: Median F1 score and ROC AUC vs rank for classification performed on principal components achieved from registered and unregistered trajectories. Registration seems to reduce required rank for higher classification accuracy.

Algorithm	Median F1 Score	95% Confidence Interval
Euclidean KNN	0.7272	(0.56, 0.8484)
DTW + KNN ([34])	0.7619	(0.5923, 0.8888)
PCA on Joint angles ([22])	0.8461	(0.7142, 0.9375)
Rotational registration to healthy via SVD ([41])	0.7741	(0.6313, 0.8914)
Functional PCA Kendall	0.88	(0.75, 0.96)

Table 4.1: Performance comparison for different algorithms based on k-nearest neighbors in order to understand effect of distances on classification performance.

Algorithm	Median F1 Score	95% Confidence Interval
Functional pca kinematic (unaligned)	0.80	(0.67, 0.90)
Functional shape pca kinematic	**0.88**	**(0.75, 0.96)**
Functional pca emg (unaligned)	0.67	(0.53, 0.78)
Functional shape pca emg	**0.97**	**(0.92, 1.00)**
Functional pca kinematic+emg (unaligned)	0.71	(0.55, 0.83)
Functional shape pca kinematic+emg	**0.97**	**(0.92, 1.00)**

Table 4.2: Performance comparison for different algorithms with and without alignment.

4.5 Discussion

This study introduces a novel method for analyzing biomechanical gait data that mitigates the influence of nuisance parameters like rotations and translations. This approach leverages joint shape space for alignment, enabling the extraction of the underlying periodic structure from kinematic and EMG data, revealing valuable information about gait patterns.

The effectiveness of the method is demonstrated in two key ways. First, it achieves superior phase matching between source and target sequences compared to existing methods, leading to more accurate comparisons. Second, the registration facilitates the identification of distinct clusters separating healthy and stroke patients based on pairwise distance measures and Multi-Dimensional Scaling. This clear separation is crucial for effective diagnosis and analysis, which is often hampered by traditional registration methods.

By applying this registration method and subsequent functional PCA on the gait data, we uncover clinically relevant gait characteristics that differentiate healthy individuals from stroke patients. The analysis reveals reduced knee flexion, shorter stride length, and less hand sway in stroke patients. Further analysis using functional PCA identifies specific components that correlate with clinical metrics, providing valuable insights into gait abnormalities. Notably, one component exhibits a strong correlation with stroke laterality.

The method is useful to clinicians for several reasons: Joint PCA (Principal Component Analysis) applied to EMG and kinematic (motion shapes) data enables clinicians and researchers to uncover meaningful patterns in stroke rehabilitation, particularly when analyzing naturalistic data. This approach allows for a comprehensive assessment of motor function recovery by integrating information about movement patterns (kinematics) and muscle activation (EMG) simultaneously.

In naturalistic settings, stroke patients often exhibit variability in their movement speeds, starting positions, and overall execution of tasks. Traditional analytical methods may struggle to account for these variations. However, joint PCA addresses these challenges by consolidating information from both kinematic and EMG datasets into a unified framework. This integration enables the identification of coherent patterns that may not be discernible when each modality is analyzed independently.

For instance, joint PCA can reveal clusters of patients who exhibit similar gait patterns (kinematics) alongside consistent patterns of muscle activation (EMG). These patterns may indicate shared underlying mechanisms of recovery or response to rehabilitation interventions. By reducing the dimensionality of complex data while preserving the most significant sources of variation, joint PCA facilitates the extraction of interpretable modes that are crucial for understanding motor function dynamics post-stroke.

In conclusion, this method offers a powerful tool for analyzing biomechanical gait data. By removing nuisance parameter variations and revealing underlying gait characteristics, this method has the potential to significantly improve stroke diagnosis, assessment, and rehabilitation strategies. Future work will explore the application of this registration method to larger patient cohorts and investigate its ability to monitor treatment progress in stroke patients.

Chapter 5

Conclusions

In this dissertation, we explored the application of shape analysis in two distinct biomechanical contexts: stroke survivors and children with Neuromuscular Disorders (NMDs). Our primary aim was to address the limitations of existing methods, which are often subjective and lack standardized outcome measures.

Our initial study introduces a novel, interpretable approach for assessing motor function in children with neuromuscular disorders. We utilize shape analysis to extract meaningful features from motion trajectories captured by wearable sensors. Functional principal component analysis (FPCA) is employed to identify key patterns in these trajectories, highlighting distinct scaling and asymmetry modes across various daily activities. Furthermore, canonical correlation analysis (CCA) uncovers a covariation mode significantly correlated with established clinical measures such as muscle fat infiltration, dynamometry-derived strength, Brooke's score (an existing motor function index), and age. This CCA-derived mode is proposed as a novel, interpretable index of motor function, providing a clear advantage over the black-box classifiers commonly used in movement analysis.

Our findings hold significant promise for the development of home-based monitoring systems for patients with neuromuscular disorders. These systems can collect longitudinal data over extended periods, reducing the need for frequent clinic visits. This facilitates more comprehensive data collection and enables clinicians to track subtle changes in function reported by caregivers. By integrating activity recognition algorithms, these systems could provide doctors with detailed insights into a patient's functional performance across various daily activities. Additionally, the non-intrusive nature of wearable sensors makes them ideal for monitoring disease progression, particularly for patients undergoing novel therapies like gene therapy. Telemedicine using wearable sensors has the potential to expand clinical support to patients in remote areas and during public health emergencies.

We acknowledge the limitations of our study, particularly the relatively small sample size. Recruitment for this specific patient population is inherently challenging, making our cohort size noteworthy within this context. We recognize that the ”quality” of movement might not be a singular concept as patients may develop compensatory strategies to perform motions effectively. This aspect warrants further investigation to refine our approach for comprehensive motor function assessment. Future work will focus on expanding the participant pool, validating the clinical utility of the proposed index in a larger cohort, and exploring the incorporation of activity recognition for a more holistic assessment of daily function.

Our second study introduces a novel method for analyzing biomechanical gait data that mitigates the influence of nuisance parameters like rotations and translations. This approach leverages joint shape space for alignment, enabling the extraction of the underlying periodic structure from kinematic and EMG data, thereby revealing valuable information about gait patterns.

The effectiveness of the method is demonstrated in two key ways. First, it achieves superior phase matching between source and target sequences compared to existing methods, leading to more accurate comparisons. Second, the registration facilitates the identification of distinct clusters separating healthy individuals and stroke patients based on pairwise distance measures and Multi-Dimensional Scaling. This clear separation is crucial for effective diagnosis and analysis, which is often hampered by traditional registration methods.

By applying this registration method and subsequent functional PCA on the gait data, we uncover clinically relevant gait characteristics that differentiate healthy individuals from stroke patients. The analysis reveals reduced knee flexion, shorter stride length, and less hand sway in stroke patients. Further analysis using functional PCA identifies specific components that correlate with clinical metrics, providing valuable insights into gait abnormalities.

In conclusion, this method offers a powerful tool for analyzing biomechanical gait data. By removing nuisance parameter variations and revealing underlying gait characteristics, this method has the potential to significantly improve stroke diagnosis, assessment, and potentially rehabilitation strategies. Future work will explore the application of this registration method to larger patient cohorts and investigate its ability to monitor treatment progress in stroke patients. Additionally, we are interested in investigating variational autoencoders (VAEs) along with Transported Square Root Vector Fields (TSRVF) to perform nonlinear dimensionality reduction in shape spaces.

Bibliography

[1] Tamaya Van Criekinge et al. “A full-body motion capture gait dataset of 138 able-bodied adults across the life span and 50 stroke survivors”. In: *Scientific Data* 10.1 (2023), p. 852.

[2] Anuj Srivastava and Eric P Klassen. *Functional and shape data analysis.* Vol. 1. Springer, 2016.

[3] David George Kendall et al. *Shape and shape theory.* John Wiley & Sons, 2009.

[4] Boulbaba Ben Amor, Jingyong Su, and Anuj Srivastava. “Action recognition using rate-invariant analysis of skeletal shape trajectories”. In: *IEEE transactions on pattern analysis and machine intelligence* 38.1 (2015), pp. 1–13.

[5] Eric W Ottesen. “ISS-N1 makes the first FDA-approved drug for spinal muscular atrophy”. In: *Translational neuroscience* 8.1 (2017), pp. 1–6.

[6] Melissa Bowerman et al. “Therapeutic strategies for spinal muscular atrophy: SMN and beyond”. In: *Disease models & mechanisms* 10.8 (2017), pp. 943–954.

[7] Eugene H Kaji and Jeffrey M Leiden. “Gene and stem cell therapies”. In: *Jama* 285.5 (2001), pp. 545–550.

[8] Michael H Brooke et al. “Clinical trial in duchenne dystrophy. I. The design of the protocol”. In: *Muscle & Nerve* 4.3 (1981), pp. 186–197. DOI: `https://doi.org/10.1002/mus.880040304`.

[9] Allan M Glanzman et al. “Validation of the children’s Hospital of Philadelphia infant test of neuromuscular disorders (CHOP INTEND)”. In: *Pediatric Physical Therapy* 23.4 (2011), pp. 322–326.

[10] Anna Mayhew et al. “Development of the Performance of the Upper Limb module for Duchenne muscular dystrophy”. In: *Developmental Medicine & Child Neurology* 55.11 (2013), pp. 1038–1045.

[11] Valeria Ricotti et al. “Wearable full-body motion tracking of activities of daily living predicts disease trajectory in Duchenne muscular dystrophy”. In: *Nature Medicine* 29.1 (2023), pp. 95–103.

[12] Anoopum S Gupta et al. “At-home wearables and machine learning sensitively capture disease progression in amyotrophic lateral sclerosis”. In: *Nature Communications* 14.1 (2023), p. 5080.

[13] Marcin Straczkiewicz et al. “Upper limb movements as digital biomarkers in people with ALS”. In: *Ebiomedicine* 101 (2024).

[14] Brandon Oubre and Sunghoon Ivan Lee. “Detection and Assessment of Point-to-Point Movements During Functional Activities Using Deep Learning and Kinematic Analyses of the Stroke-Affected Wrist”. In: *IEEE Journal of Biomedical and Health Informatics* 28.2 (2024), pp. 1022–1030. DOI: `10.1109/JBHI.2023.3337156`.

[15] Hongjun Choi et al. “Temporal Alignment Improves Feature Quality: An Experiment on Activity Recognition with Accelerometer Data”. In: *2018 IEEE/CVF Conference on Computer Vision and Pattern Recognition Workshops (CVPRW)*. 2018, pp. 462–4628. DOI: `10.1109/CVPRW.2018.00075`.

[16] Shashwat Kumar et al. “Shape Analysis for Pediatric Upper Body Motor Function Assessment”. In: *Proceedings of the 2022 ACM International Symposium on Wearable Computers*. ISWC ’22. Cambridge, United Kingdom: Association for Computing Machinery, 2022, pp. 39–43. ISBN: 9781450394246. DOI: `10.1145/3544794.3558463`.

[17] E D Oña Simbaña et al. “Review of Automated Systems for Upper Limbs Functional Assessment in Neurorehabilitation”. In: *IEEE Access* 7 (2019), pp. 32352–32367. ISSN: 2169-3536. DOI: `10.1109/ACCESS.2019.2901814`.

[18] X Song et al. "Cellphone-Based Automated Fugl-Meyer Assessment to Evaluate Upper Extremity Motor Function After Stroke". In: *IEEE Transactions on Neural Systems and Rehabilitation Engineering* 27.10 (2019), pp. 2186–2195. ISSN: 1558-0210. DOI: 10.1109/TNSRE.2019.2939587.

[19] B Oubre et al. "Estimating Upper-Limb Impairment Level in Stroke Survivors Using Wearable Inertial Sensors and a Minimally-Burdensome Motor Task". In: *IEEE Transactions on Neural Systems and Rehabilitation Engineering* 28.3 (2020), pp. 601–611. ISSN: 1558-0210. DOI: 10.1109/TNSRE.2020.2966950.

[20] Boulbaba Ben Amor et al. "A framework for interpretable full-body kinematic description using geometric and functional analysis". In: *IEEE Transactions on Biomedical Engineering* 67.6 (2019), pp. 1761–1774.

[21] Min Chen et al. "An interpretable deep learning optimized wearable daily detection system for Parkinson's disease". In: *IEEE Transactions on Neural Systems and Rehabilitation Engineering* (2023).

[22] Jieun Cho et al. "Stroke walking and balance characteristics via principal component analysis". In: *Scientific Reports* 14.1 (2024), p. 10465.

[23] Robert Gutierrez et al. "Upper Extremity Examination for Neuromuscular Diseases (U-EXTEND): Protocol for a Multimodal Feasibility Study". In: *JMIR Res Protoc* 11.10 (Oct. 2022), e40856. DOI: 10.2196/40856.

[24] *MMR+ – METAMOTIONR+*. https://mbientlab.com/store/mmrp-metamotionrp/. Accessed: 7-10-2024.

[25] Dimitri P Bertsekas et al. "Dynamic programming and optimal control". In: *Belmont, MA: Athena Scientific* 1 (2011).

[26] J Derek Tucker, Wei Wu, and Anuj Srivastava. "Generative models for functional data using phase and amplitude separation". In: *Computational Statistics & Data Analysis* 61 (2013), pp. 50–66.

[27] Eric J Jones et al. "Cross-sectional area and muscular strength: a brief review". In: *Sports medicine* 38 (2008), pp. 987–994.

[28] Kay W. Ng, Anne M. Connolly, and Craig M. Zaidman. "Quantitative muscle ultrasound measures rapid declines over time in children with SMA type 1". In: *Journal of the Neurological Sciences* 358.1 (2015), pp. 178–182. ISSN: 0022-510X.

[29] Merel Jansen et al. "Quantitative muscle ultrasound is a promising longitudinal follow-up tool in Duchenne muscular dystrophy". In: *Neuromuscular disorders* 22.4 (2012), pp. 306–317.

[30] Abraham Wald. "Tests of statistical hypotheses concerning several parameters when the number of observations is large". In: *Transactions of the American Mathematical society* 54.3 (1943), pp. 426–482.

[31] Yoav Benjamini and Yosef Hochberg. "On the adaptive control of the false discovery rate in multiple testing with independent statistics". In: *Journal of educational and Behavioral Statistics* 25.1 (2000), pp. 60–83.

[32] F. Pedregosa et al. "Scikit-learn: Machine Learning in Python". In: *Journal of Machine Learning Research* 12 (2011), pp. 2825–2830.

[33] Skipper Seabold and Josef Perktold. "statsmodels: Econometric and statistical modeling with python". In: *9th Python in Science Conference*. 2010.

[34] Paolo Tormene et al. "Matching incomplete time series with dynamic time warping: an algorithm and an application to post-stroke rehabilitation". In: *Artificial intelligence in medicine* 45.1 (2009), pp. 11–34.

[35] Hyun-Seob Lee. "Application of dynamic time warping algorithm for pattern similarity of gait". In: *Journal of exercise rehabilitation* 15.4 (2019), p. 526.

[36] Zhe Zhang, Qiang Fang, and Xudong Gu. "Objective Assessment of Upper-Limb Mobility for Poststroke Rehabilitation". In: *IEEE Transactions on Biomedical Engineering* 63.4 (2016), pp. 859–868. DOI: 10.1109/TBME.2015.2477095.

[37] Sounak Chakraborty et al. “Functional modeling of pedaling kinematics for the Stroke patients”. In: *Journal of Biopharmaceutical Statistics* 30.4 (2020), pp. 674–688.

[38] Shir Kashi et al. “A machine-learning model for automatic detection of movement compensations in stroke patients”. In: *IEEE Transactions on Emerging Topics in Computing* 9.3 (2020), pp. 1234–1247.

[39] Sheng Li. “Stiff knee gait disorders as neuromechanical consequences of spastic hemiplegia in chronic stroke”. In: *Toxins* 15.3 (2023), p. 204.

[40] Nadia Hosni et al. “3D gait recognition based on functional PCA on Kendall’s shape space”. In: *2018 24th International Conference on Pattern Recognition (ICPR)*. IEEE. 2018, pp. 2130–2135.

[41] Nadav Eichler et al. “3D motion capture system for assessing patient motion during Fugl-Meyer stroke rehabilitation testing”. In: *IET Computer Vision* 12.7 (2018), pp. 963–975.